Integral pulse height distribution
(curva di conteggio)

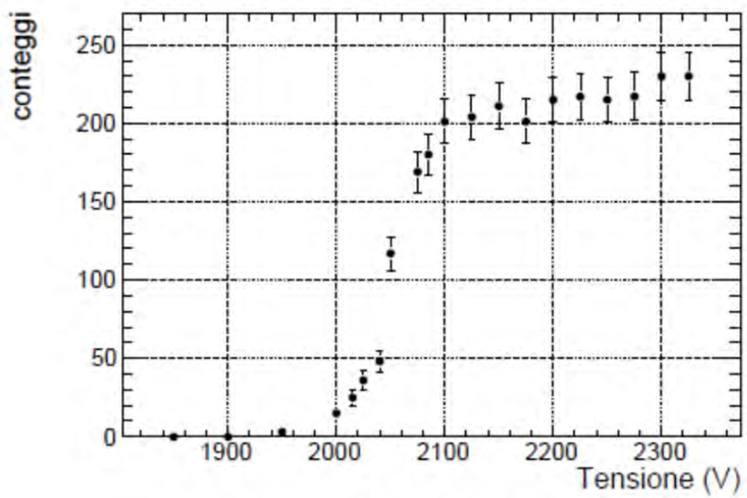

(a) PMT 2, soglia a 40 mV

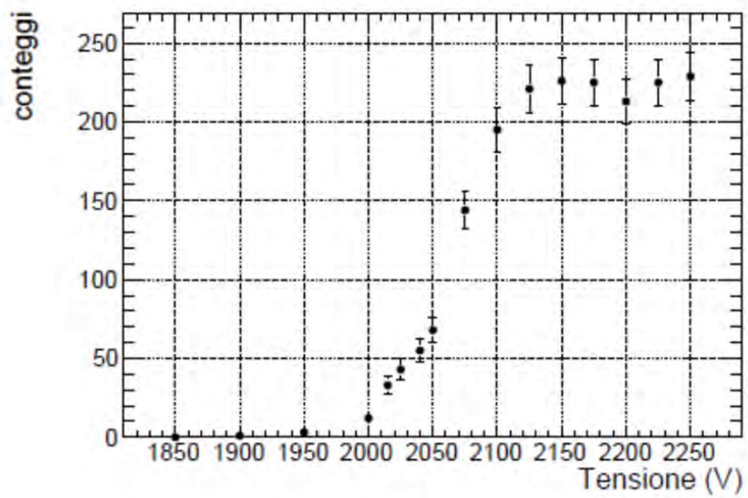

(b) PMT 2, soglia a 45 mV

at determines Resolution?

gnal Variance >> Baseline Variance

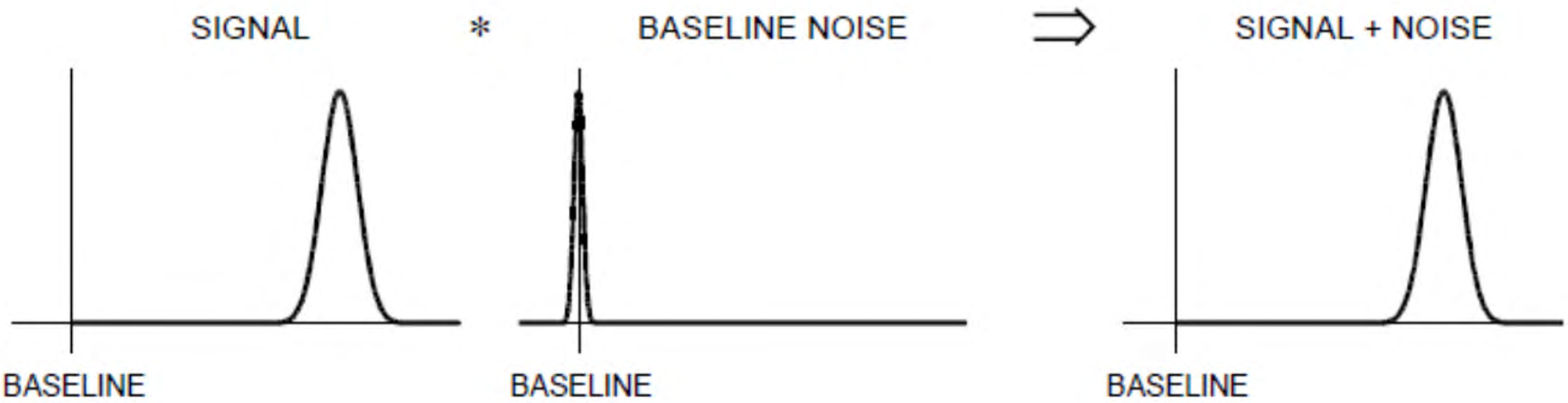

⇒ Electronic (baseline) noise not important

Examples:
- High-gain proportional chambers
- Scintillation Counters with High-Gain PMTs

e.g. 1 MeV γ-rays absorbed by NaI(Tl) crystal

Number of photoelectrons: $N_{pe} \approx 8{\cdot}10^4\ [\text{MeV}^{-1}] \times E_\gamma \times QE \approx 2.4{\cdot}10^4$

Variance typically: $\sigma_{pe} = N_{pe}^{1/2} \approx 160$ and $\sigma_{pe} / N_{pe} \approx 5 - 8\%$

Signal at PMT anode (assume Gain= 10^4): $Q_{sig} = G_{PMT} N_{pe} \approx 2.4{\cdot}10^8$ el and
$\sigma_{sig} = G_{PMT}\, \sigma_{pe} \approx 1.2{\cdot}10^7$ el

whereas electronic noise easily $< 10^4$ el nal Variance << Baseline Variance

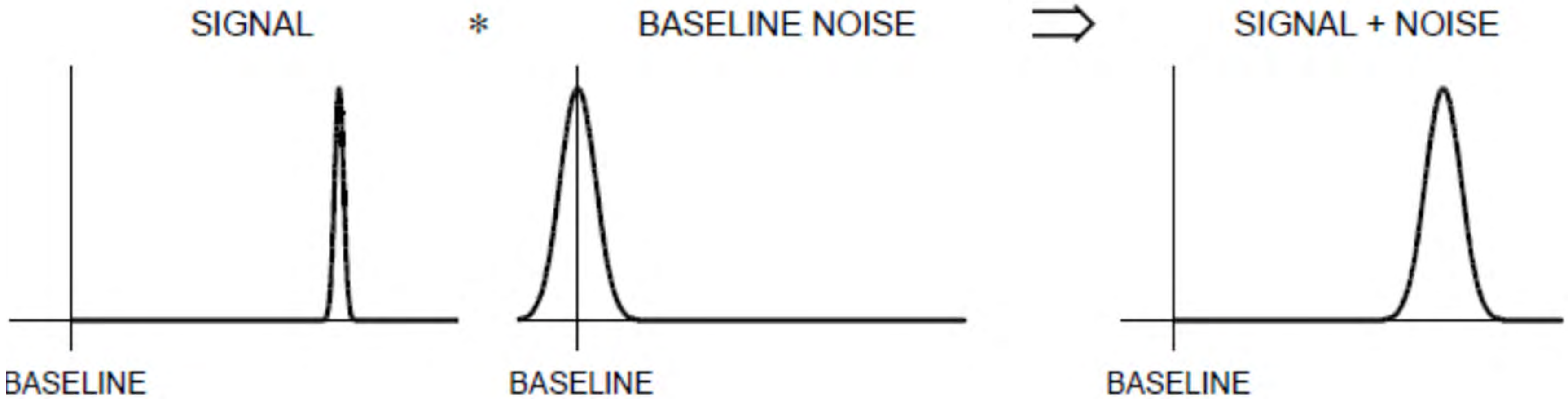

⇒ Electronic (baseline) noise critical for resolution

Examples:
- Gaseous ionization chambers (no internal gain)
- Semiconductor detectors

e.g. in Si : Number of electron-hole pairs $N_{ep} = \dfrac{E_{dep}}{3.6 \text{ eV}}$

Variance $\sigma_{ep} = \sqrt{F \cdot N_{ep}}$ (where F= Fano factor $\approx$ 0.1)

For 50 keV photons: $\sigma_{ep} \approx 40$ el $\Rightarrow$ $\sigma_{ep} / N_{ep} = 7.5 \cdot 10^{-4}$

Obtainable noise levels are 10 to 1000 el.

Baseline fluctuations can have many origins ...

pickup of external interference

artifacts due to imperfect electronics

… etc.,

but the (practical) fundamental limit is electronic noise.

1.10 Detection limits and resolution

In addition to signal fluctuations originating in the sensor, the minimum detection limit and energy resolution are subject to fluctuations introduced by the electronics. The gain can be controlled very precisely, but electronic noise introduces baseline fluctuations, which are superimposed on the signal and alter the peak amplitude. Figure 1.24 (left) shows a typical noise waveform. Both the amplitude and time distributions are random.

When superimposed on a signal, the noise alters both the amplitude and time dependence. Figure 1.24 (right) shows the noise waveform superimposed on a small signal. As can be seen, the noise level determines the minimum signal whose presence can be discerned.

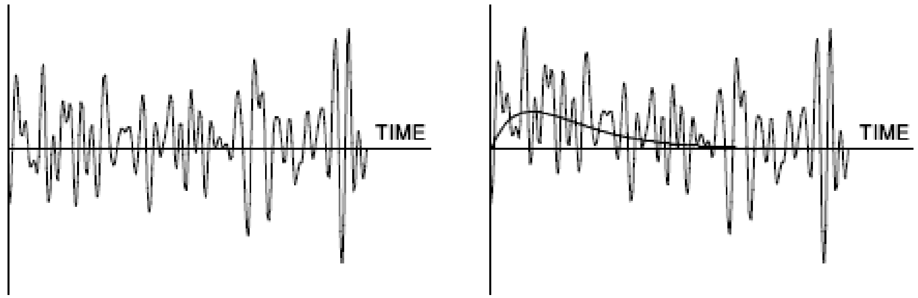

FIG. 1.24. Waveforms of random noise (left) and signal + noise (right), where the peak signal is equal to the rms noise level ($S/N = 1$). The noiseless signal is shown for comparison.

Spectroscopy:

- Experiments to determine the decay products of excited states and their interaction
- The excitation energies of a system increase as size decrease. To produce these excited states high energy particles are needed.

Absolute energies may vary a lot But resolution usually still a critical issue

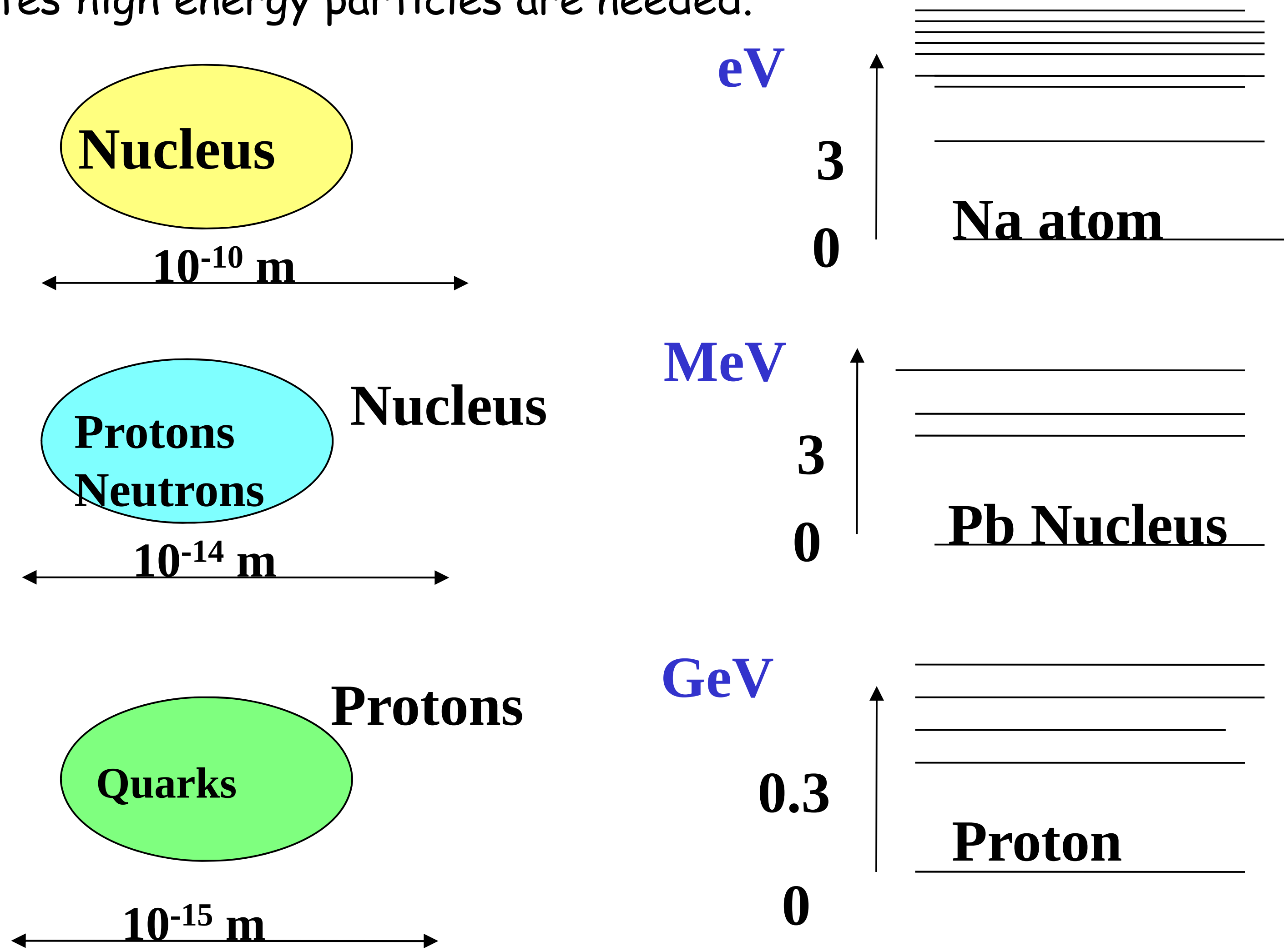

esolution and Electronic Noise

lution: the ability to
guish signal levels

hy?

ecognize structure in amplitude spectra

Comparison between NaI(Tl)
and Ge detectors

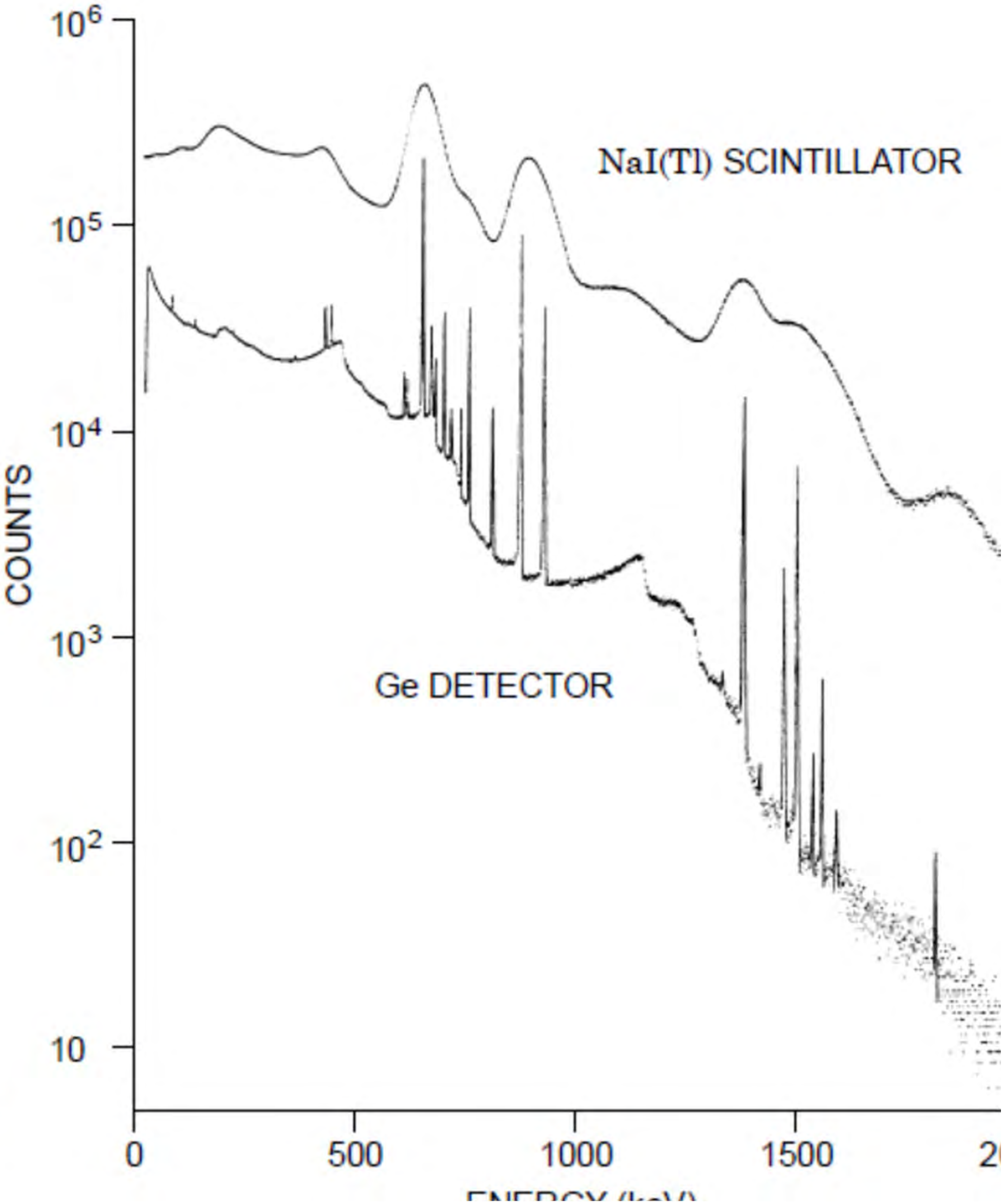

. Philippot, IEEE Trans. Nucl. Sci. **NS-17/3** (1970) 446

b) Improve sensitivity

Signal to background ratio improves with better resolution

(signal counts in fewer bins compete with fewer background counts)

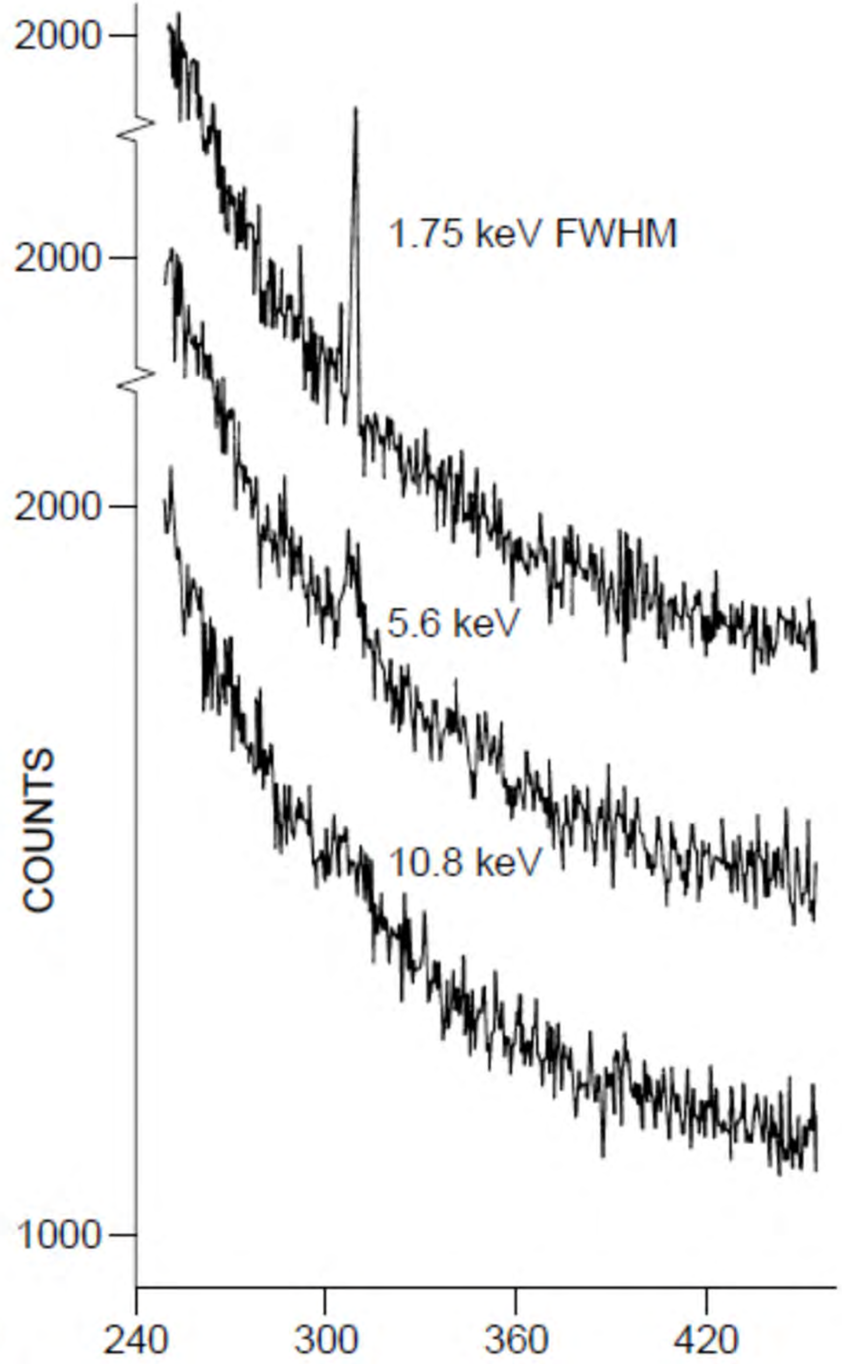

G.A. Armantrout *et al.*, IEEE Trans. Nucl. Sci. **NS-19/1** (1972) 107

li di Frascati of INFN, wh
next year. The experiment,
ram, has some special f
ypernuclear physics experi
vill operate at a e^+e^- collide
Vhat follows will describe i

tructure of Λ–hypernuc

Λ-hypernucleus ${}^A_\Lambda Z$ is a bo
rons and a Λ hyperon. Th
nade by the (A-1) nucleons
ne nucleus ${}^{(A-1)}Z$ and the
he Λ hyperon, carrying th
istinguishable baryon an
nposed by the Pauli princi
um states already filled up v
hyperon, embedded in a
xplore nuclear structure.

The binding energy B_Λ of
its ground state is defined

$$B_\Lambda = M$$

here M_{core} is the mass (in
ie mass of the Λ particle an
Z, experimentally measu
ope of about 1 MeV/(unit
r the heavy hypernuclei. Th
which the Λ particle is con
qual to the nuclear radius an
the 55 MeV typical value c

This is consistent with a Λ-
icleon-nucleon one. Indeec
teraction, the zero isospir
ovector mesons like the π or the ρ with a nucleon and deter-
ines the lack of strong tensor components in the interaction.
ie relative weakness of the Λ-nucleon interaction entails that the
ell structure is not disrupted by the insertion of the Λ in the
icleus and the lack of Pauli effects allows all the nuclear single
rticle states to be populated by the Λ. In Figure 2, the so called
egrè table" of the hypernuclei shows the 35 hypernuclei known
present.

Experiments of hypernucleus production by "*strangeness change*" and "*associated production*" processes can produce
pernuclei in which the Λ populates different single particle
ites. The latter technique is particularly suitable for populating
v lying Λ states, thanks to the high recoil momentum trans-
red to the Λ particle in the reaction.

A beautiful representation of this process is given in Figure 3,
iere the excitation spectrum of ${}^{89}_\Lambda Y$, obtained by the "*associated*
oduction" reaction ${}^{89}Y(\pi^+, K^+)\,{}^{89}_\Lambda Y$ at the KEK laboratory in
oan, is shown. The spectrum demonstrates how, starting from
ieutron in the $g_{9/2}$ state, it is possible to accommodate a Λ particle
the hypernuclear states f, d, p and even in the ground state s.

These measurements constitute the spectacular confirmation,
a textbook level, of the validity of the independent particle
odel or shell model of the nucleus. In non-strange nuclei, the
servation of single particle states is only possible for the states
the most external nucleon orbits. In fact, due to the Pauli prin-
le and pairing interactions, deeply bound nucleon single
rticle states are so fragmented as to be essentially unobservable.
e present experimental data on hypernuclear binding energies
d detailed spectroscopic features are limited in quantity and

tion of the *YN* interaction.

Figure 4 reports a recent measurement of the splitting of the $5/2^+$-$3/2^+$ doublet in ${}^9_\Lambda Be$ by the BNL-AGS E930 experiment [4], measuring γ rays emitted in the nuclear transitions with the new germanium detector array Hyperball. This new technique allowed the energy resolution on low lying hypernuclear levels to be improved from a few MeV to a few keV, even if the count rate resulting is still quite low, ~200 γ's per month of data taking. The spacing of the two levels was measured to be 31 ± 2 keV, incompatible with the prediction of the meson exchange models.

state nucleon in all but the l
mesonic decay modes of t
through the weak interac
($\Lambda + n \rightarrow n + n + 176$ MeV
process is possible only in hyp
of Λ's, stable against the mes
which is available inside a hy

The study of the non-mes
importance, since it provide
four fermion, strangeness ch

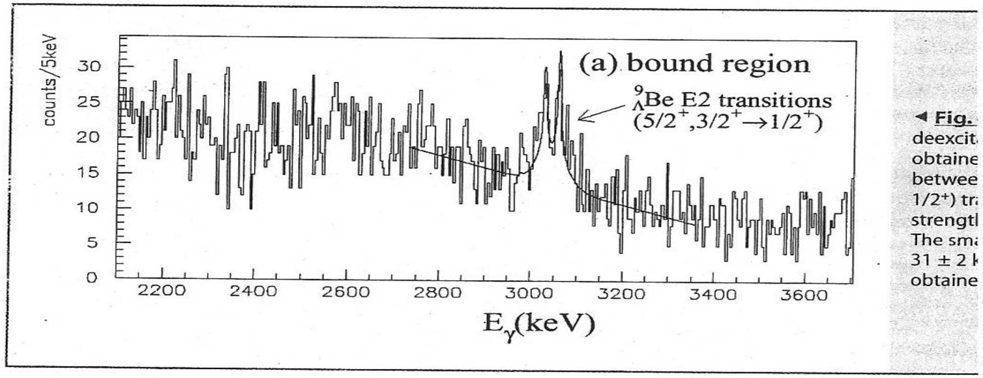

◄ Fig.
deexcit
obtaine
betwee
$1/2^+$) tr
strengt
The sm
31 ± 2 k
obtaine

The improvement of the YN interaction models would need
precise data on the free *YN* interaction, which are very difficult to

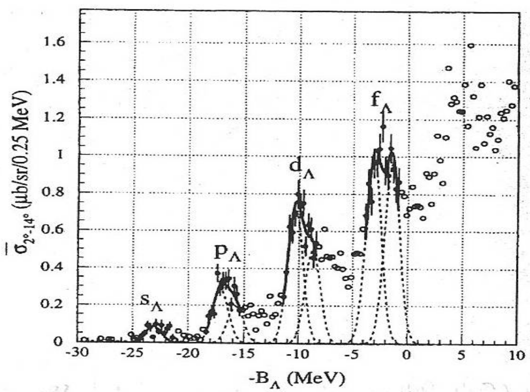

▲ Fig. 3: Hypernuclear mass spectrum of ${}^{89}_\Lambda Y$ obtained at KEK by the E369 experiment, with an energy resolution of 1.65 MeV. The bump structures correspond to the Λ major shells orbits (s, p, d, f) in the bound region. The widths of the bumps for the p-, d- and f-orbits are significantly wider than the experimental resolution and the peak for the f_Λ-orbit is split into two peaks.

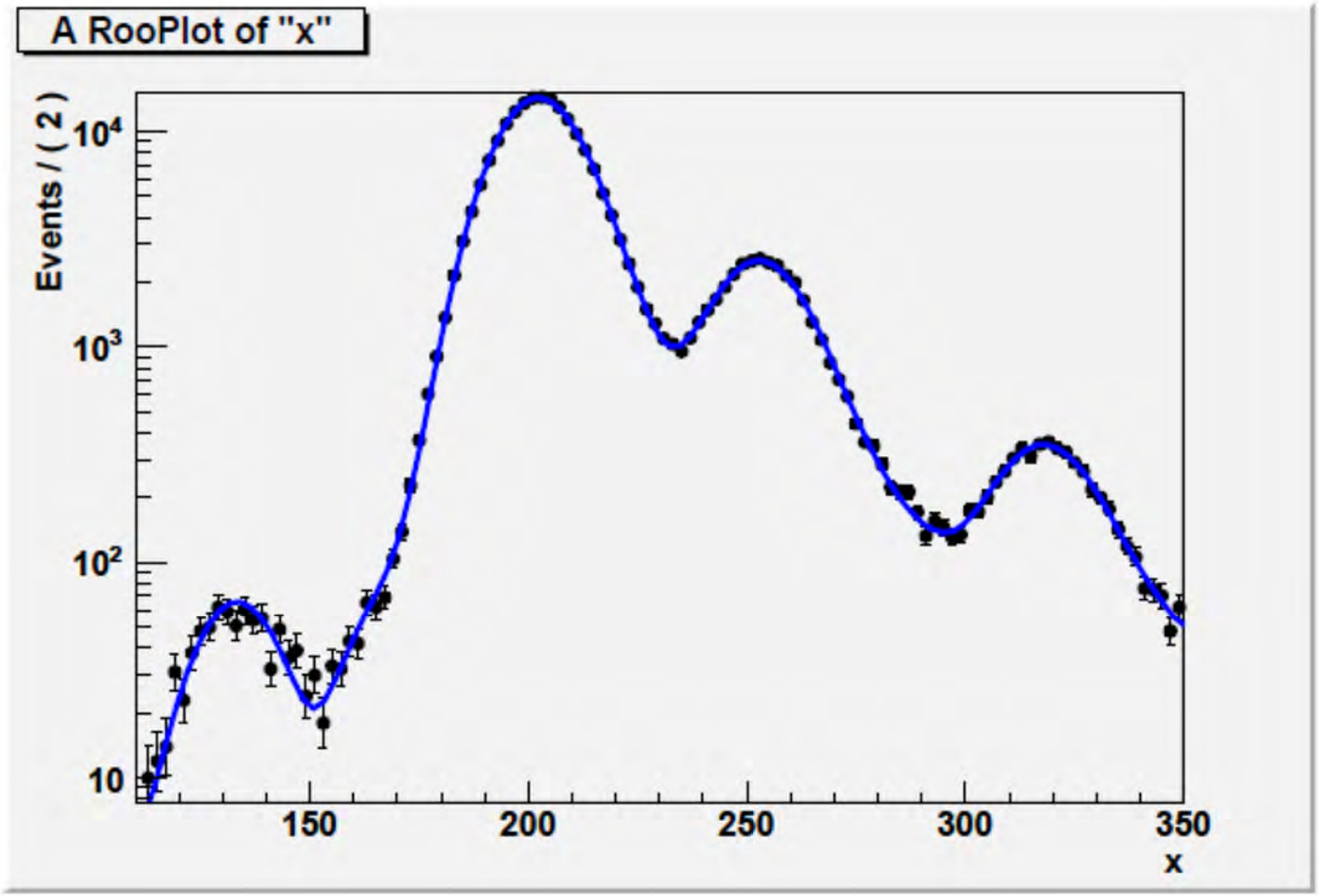

A RooPlot of "x"
Events / (2)
10^4
10^3
10^2
10
150
200
250
300
350
x

Response function

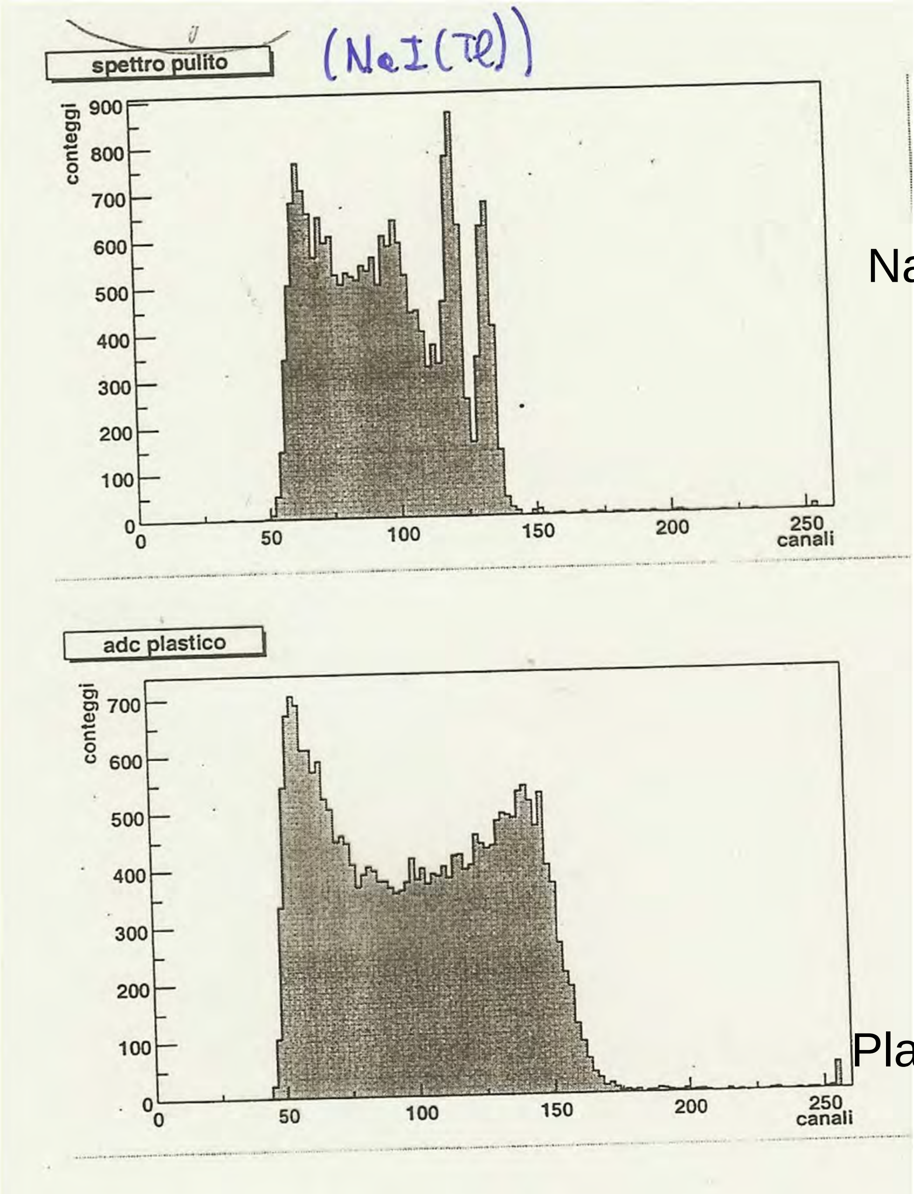

NaI(Tl) scintillator

Plastic scintillator

There are actually 2 monoenergetic radiation Sources…

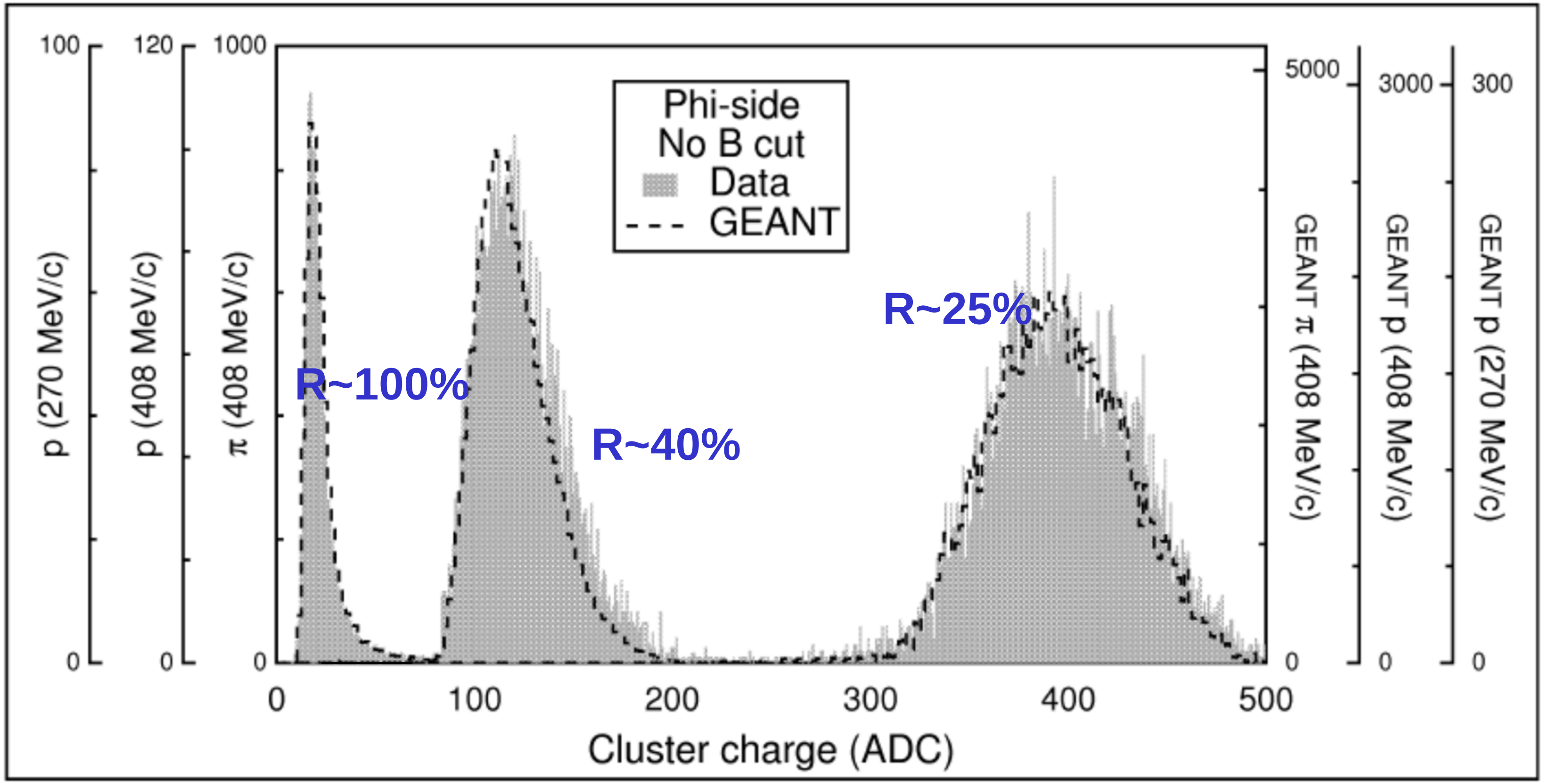

Phi-side
No B cut
Data
GEANT
R~100%
R~40%
R~25%
p (270 MeV/c)
p (408 MeV/c)
π (408 MeV/c)
GEANT π (408 MeV/c)
GEANT p (408 MeV/c)
GEANT p (270 MeV/c)
Cluster charge (ADC)

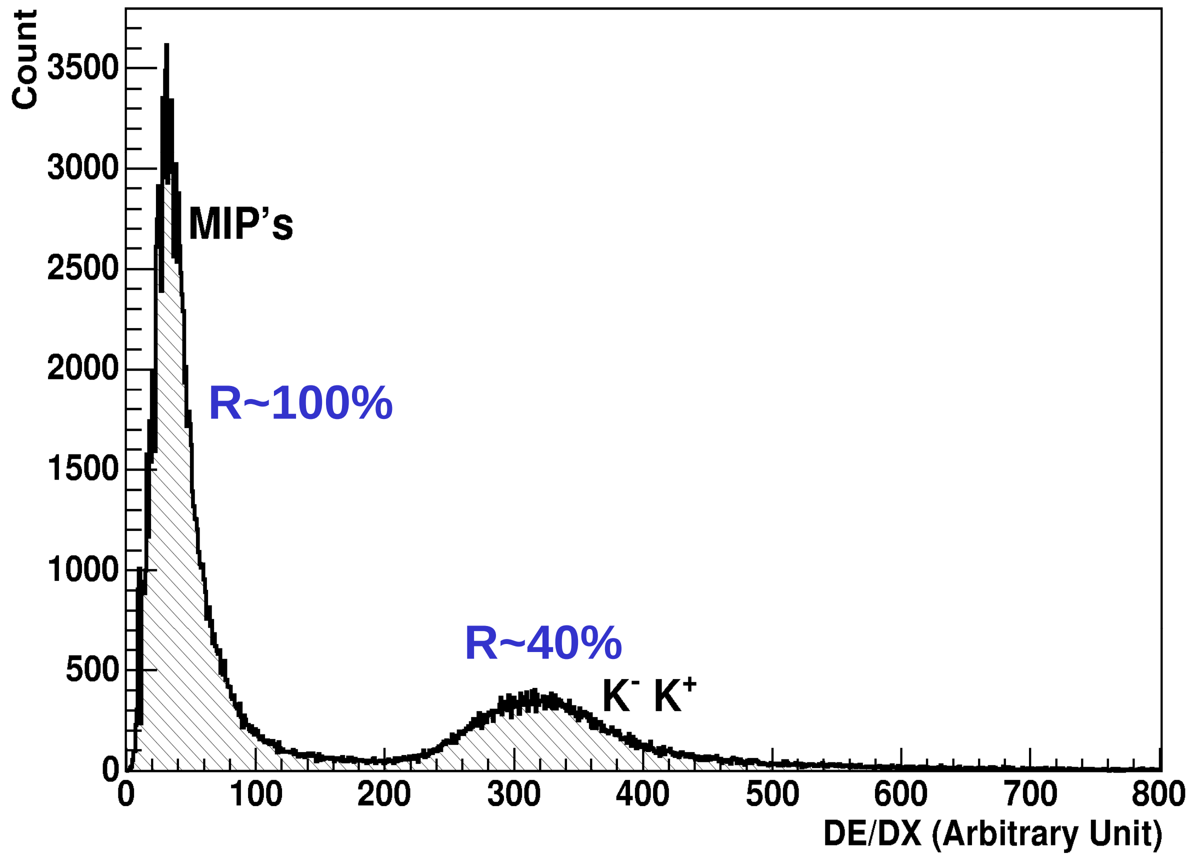

Count
3500
3000
2500
2000
1500
1000
500
0
MIP's
R~100%
R~40%
K- K+
0
100
200
300
400
500
600
700
800
DE/DX (Arbitrary Unit)

Acceptance effect on proton momentum distribution

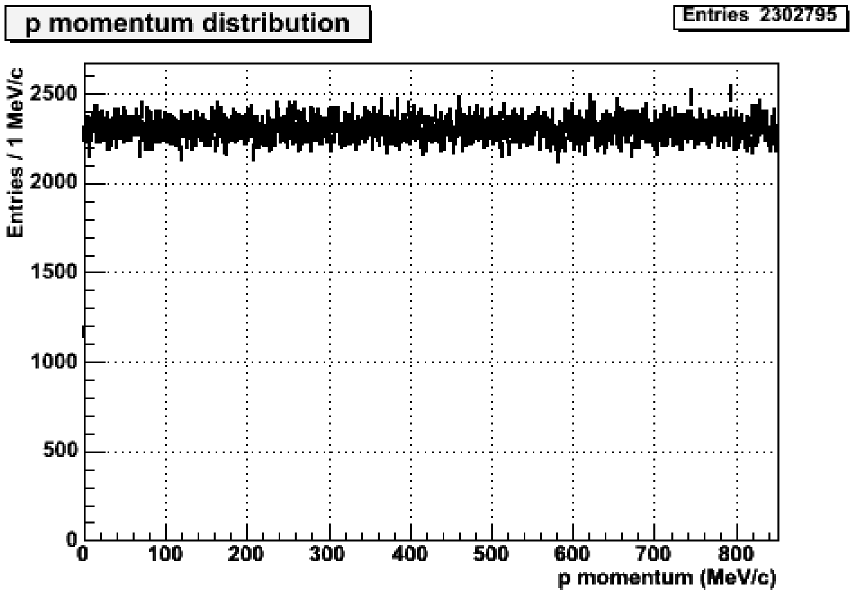

Original distribution

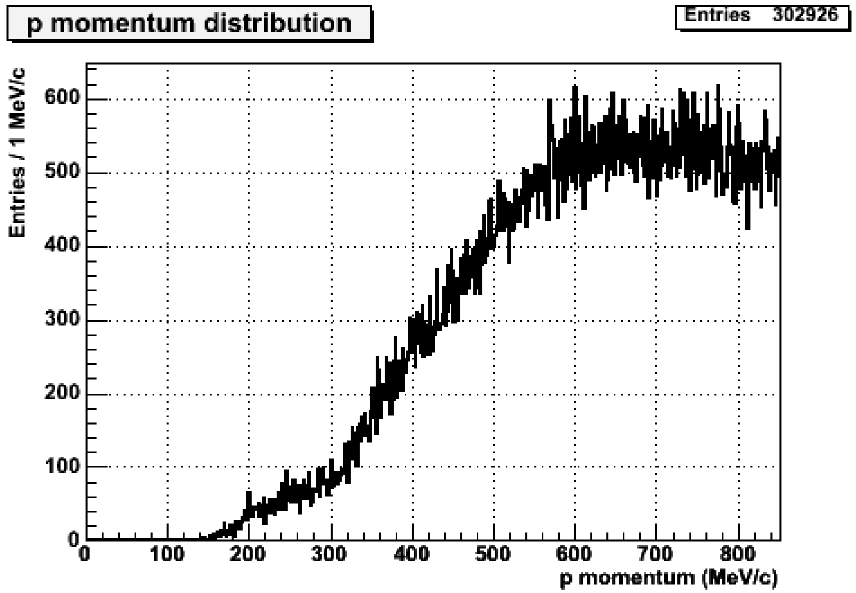

Reconstructed distribution

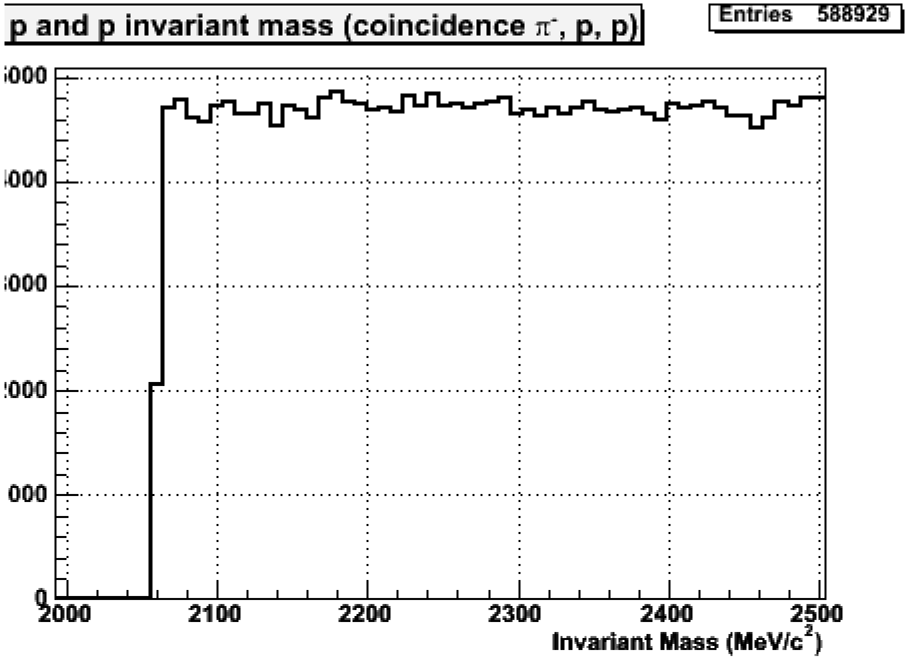
p and p invariant mass (coincidence π-, p, p)
Entries 588929
Invariant Mass (MeV/c2)
2000
2100
2200
2300
2400
2500

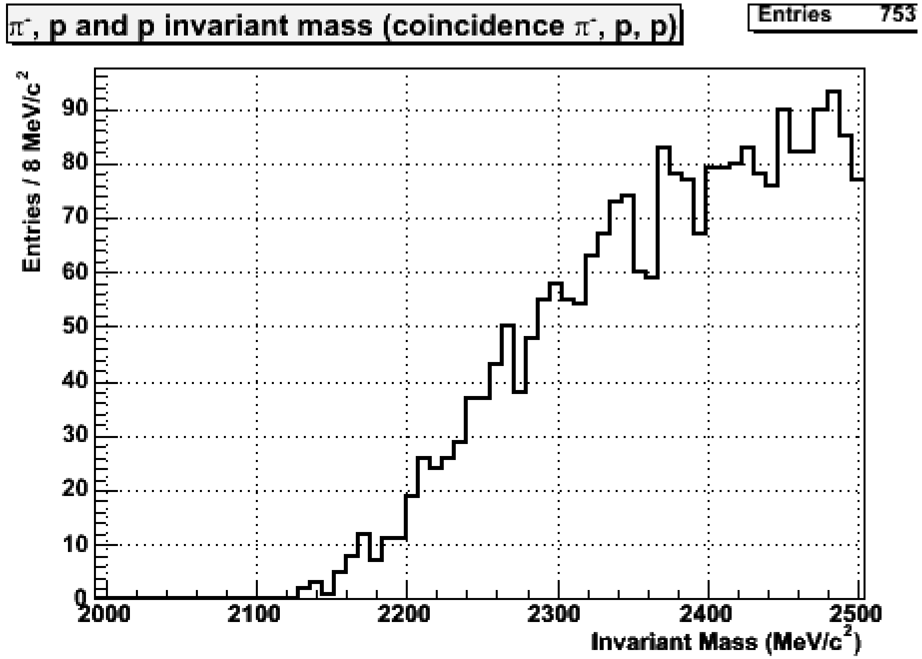
π-, p and p invariant mass (coincidence π-, p, p)
Entries 753
Entries / 8 MeV/c2
Invariant Mass (MeV/c2)
0
10
20
30
40
50
60
70
80
90
2000
2100
2200
2300
2400
2500

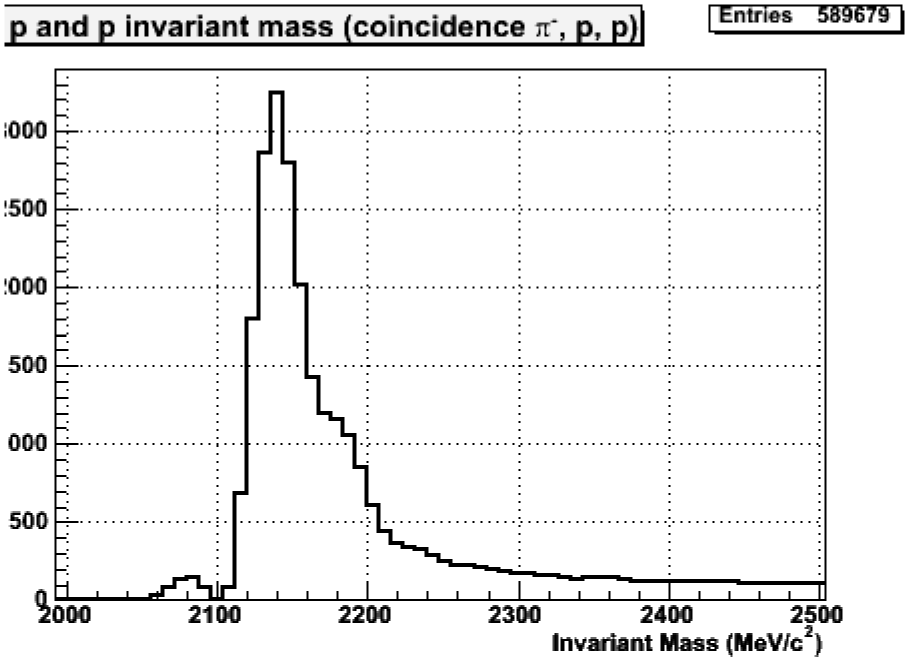
p and p invariant mass (coincidence π-, p, p)
Entries 589679
Invariant Mass (MeV/c2)
0
500
2000
2100
2200
2300
2400
2500

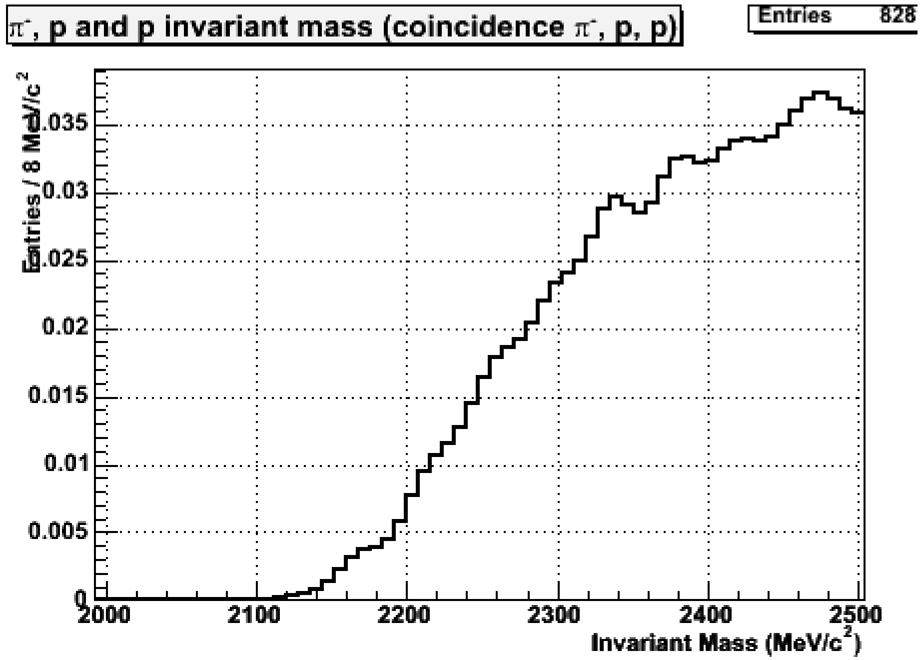
π-, p and p invariant mass (coincidence π-, p, p)
Entries 828
Entries / 8 MeV/c2
Invariant Mass (MeV/c2)
0
0.005
0.01
0.015
0.02
0.025
0.03
0.035
2000
2100
2200
2300
2400
2500

Λp acceptance

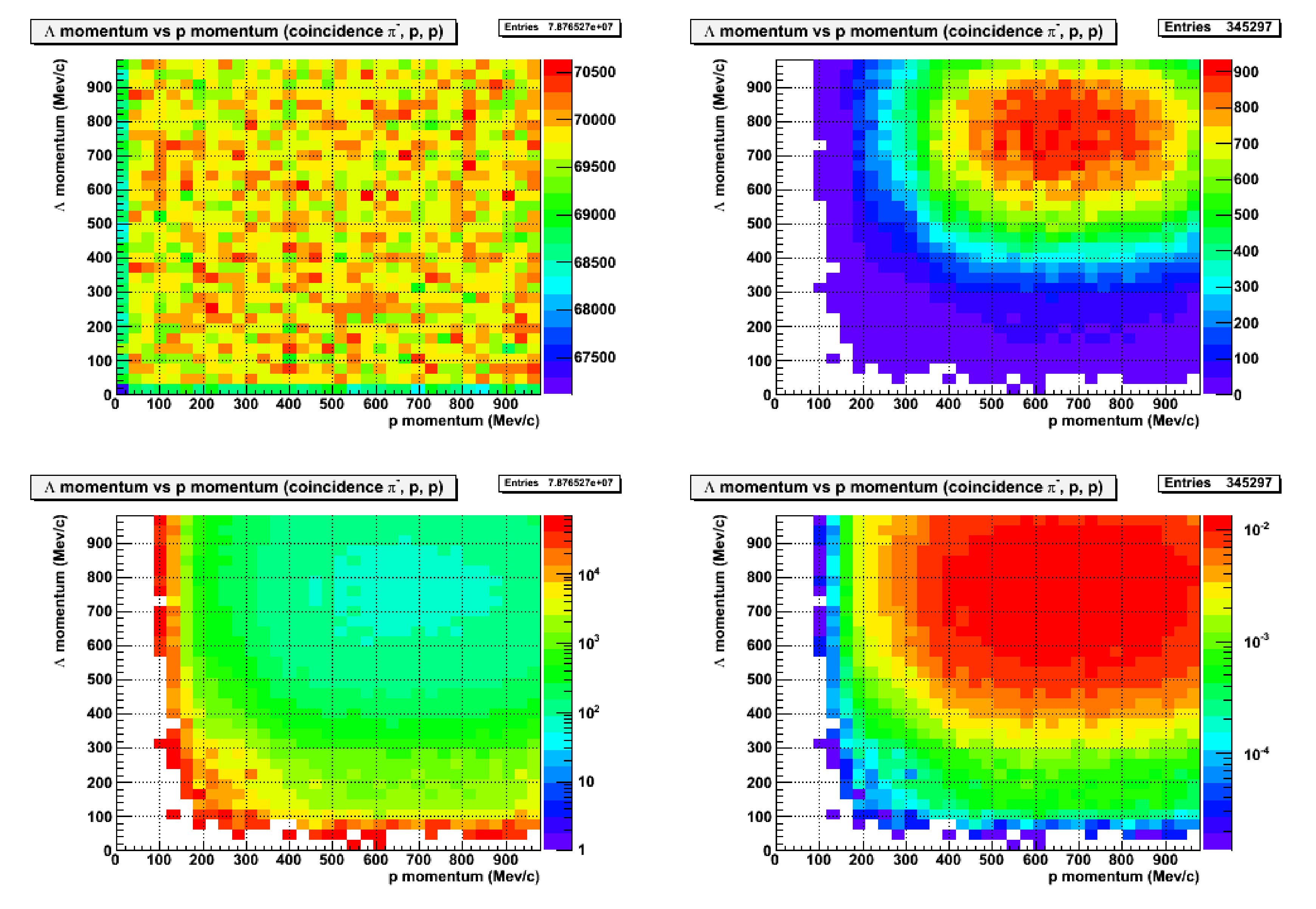

Dead time measurements

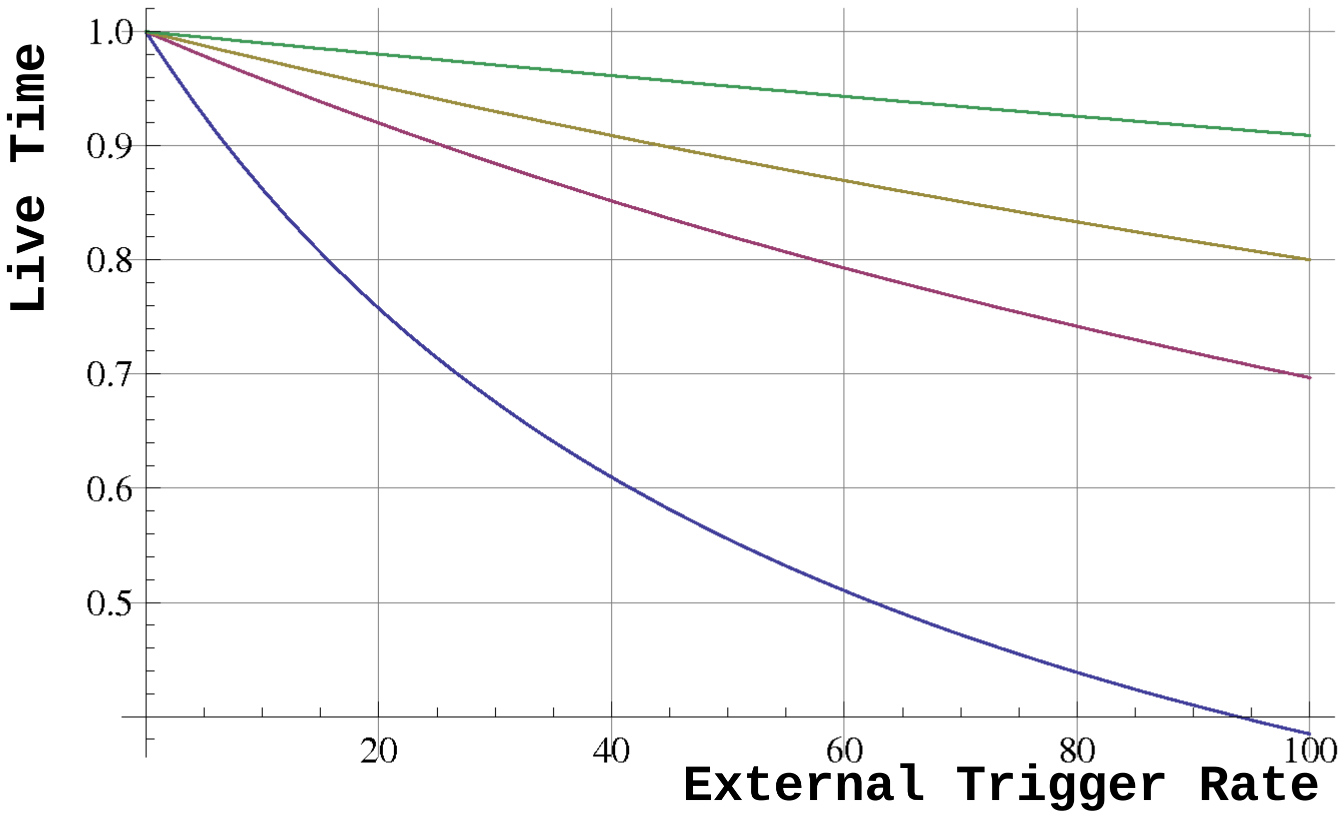

Live time= $1-T_{dead}/T$

TOF difference needed to mass discriminate particles

Figure 7.13 The time difference per unit flight path for πK, Kp, and πp as a function of momentum.

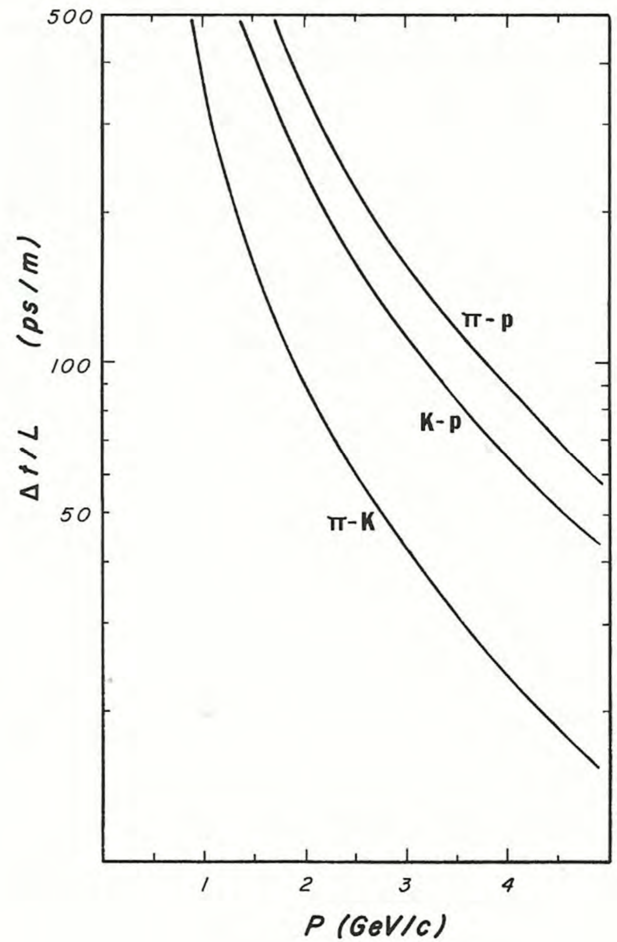

How a shower looks like

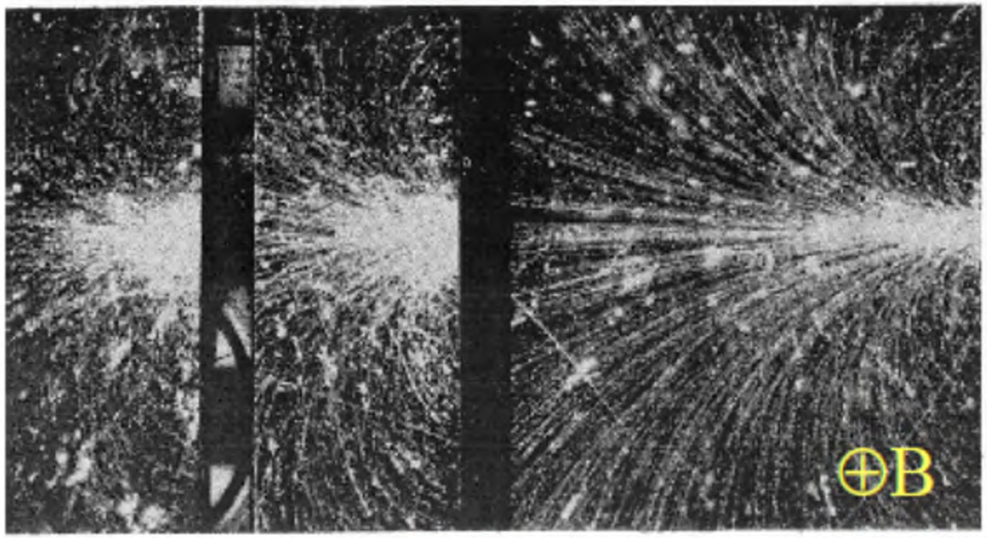

Electron shower in lead. 7500 gauss in cloud chamber. CALTECH

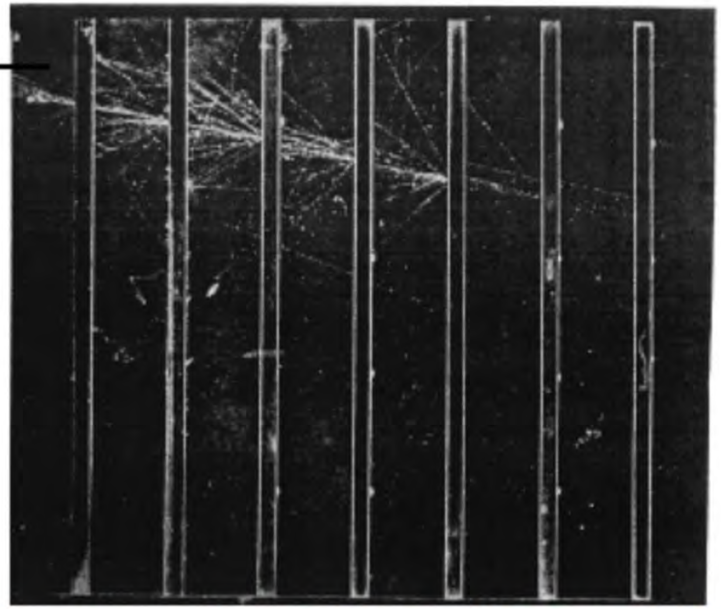

Electron shower in lead. Cloud chamber. W.B. Fretter, UCLA

Electron showers

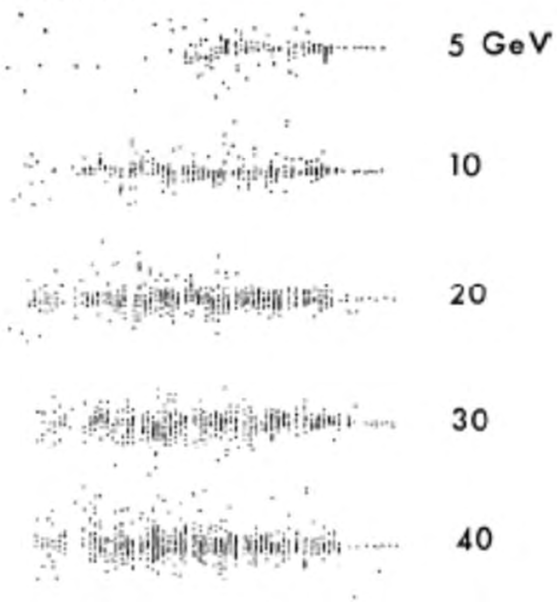

Hadron showers

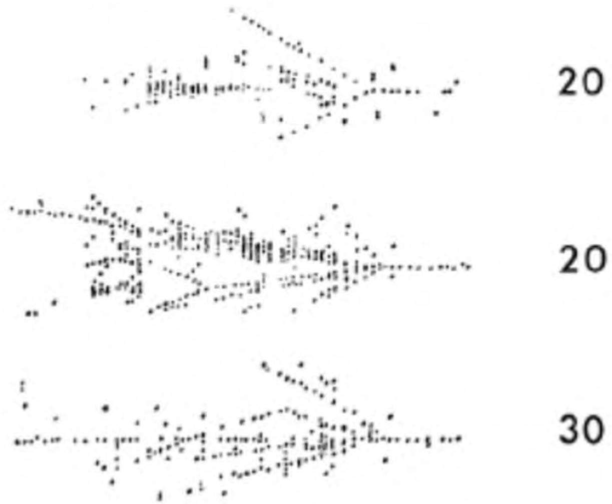

F.E. Taylor et al., IEEE NS 27(1980)30

O. Ullaland/2006

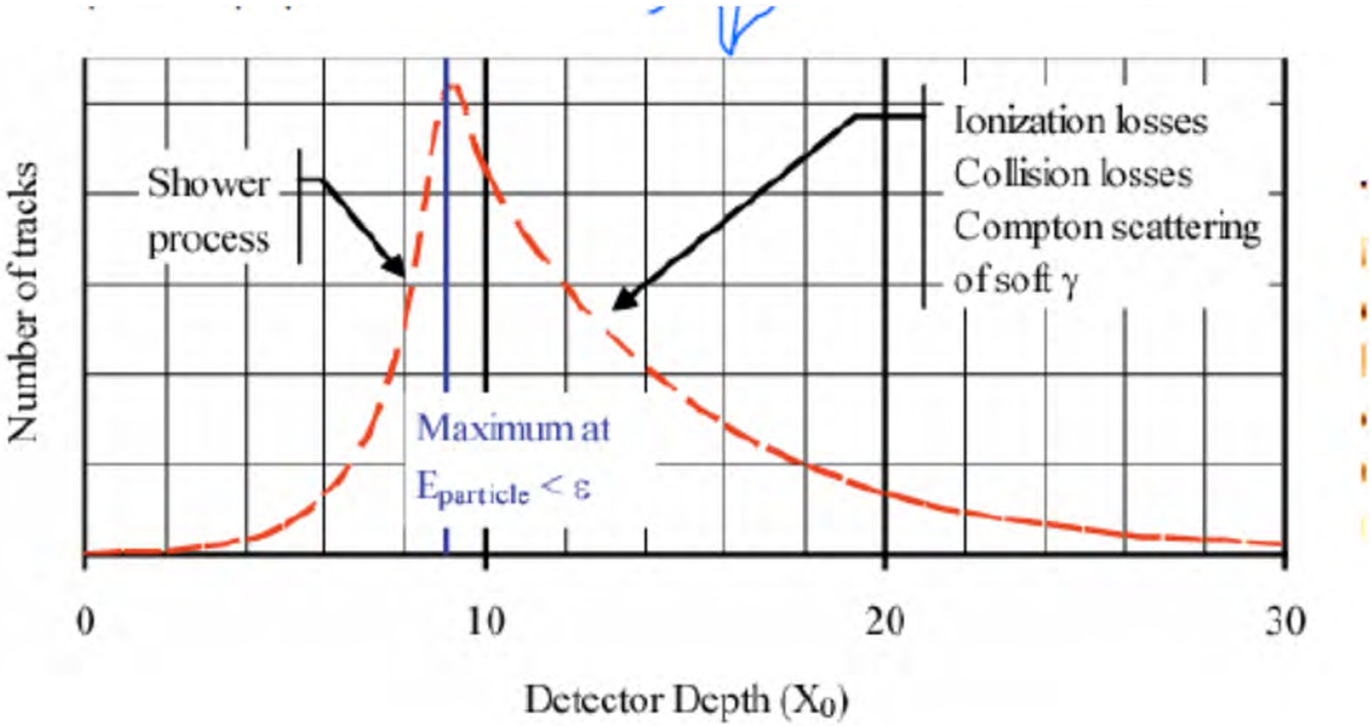
Number of tracks
Shower process
Maximum at
$E_{particle} < \varepsilon$
Ionization losses
Collision losses
Compton scattering
of soft γ
0
10
20
30
Detector Depth (X_0)

EM showers: longitudinal profile

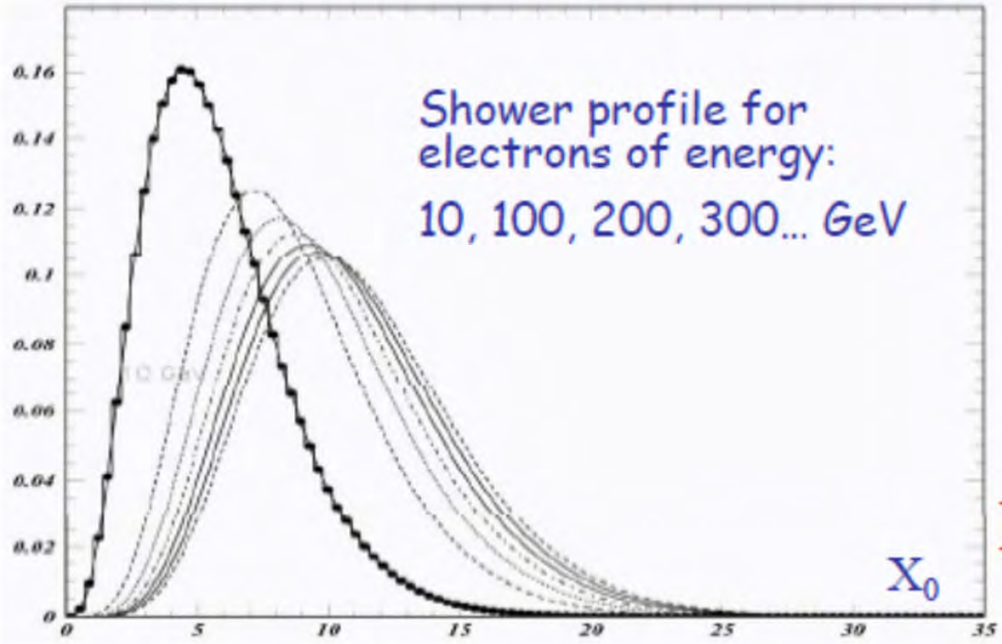

$$t_{max} = 1.4 \ln(E_0/E_c)$$

$$N_{tot} \propto E_0/E_c$$

Longitudinal containment:

$$t_{95\%} = t_{max} + 0.08Z + 9.6$$

$\mathbf{E_c \propto 1/Z}$ ⇒
- shower max
- shower tail

Shower parametrization

$$\frac{dE}{dt} \propto t^{\alpha} e^{\beta t}$$

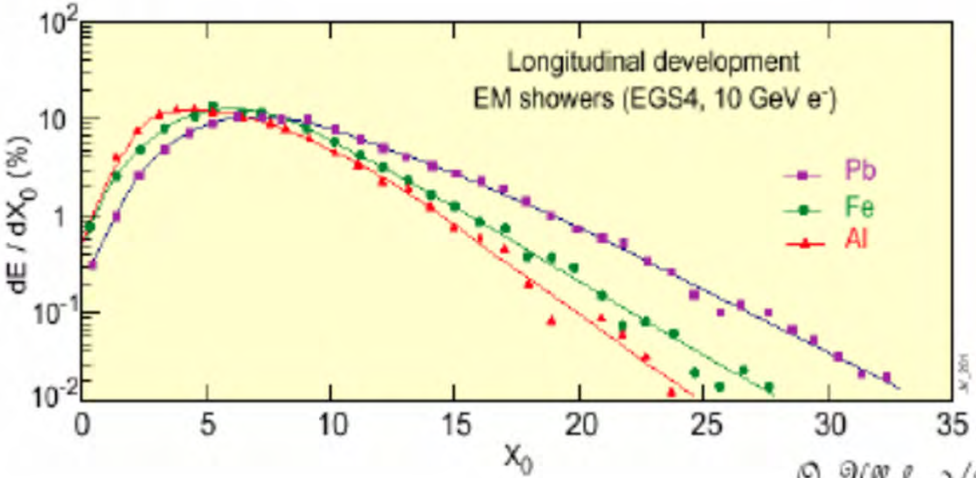

From M. Diemoz, Torino 3-02-05

O. Ullaland/2006

EM showers: transverse profile

Transverse shower profile

- Multiple scattering make electrons move away from shower axis
- Photons with energies in the region of minimal absorption can travel far away from shower axis

Molière radius sets transverse shower size, it gives the average lateral deflection of critical energy electrons after traversing $1X_0$

$$R_M = \frac{21\mathrm{MeV}}{E_C} X_0 \qquad R_M \propto \frac{X_0}{E_C} \propto \frac{A}{Z} (Z >> 1)$$

75% E_0 within $1R_M$, 95% within $2R_M$, 99% within $3.5R_M$

20 GeV γ in copper (simulation)

charged particles only

all particles

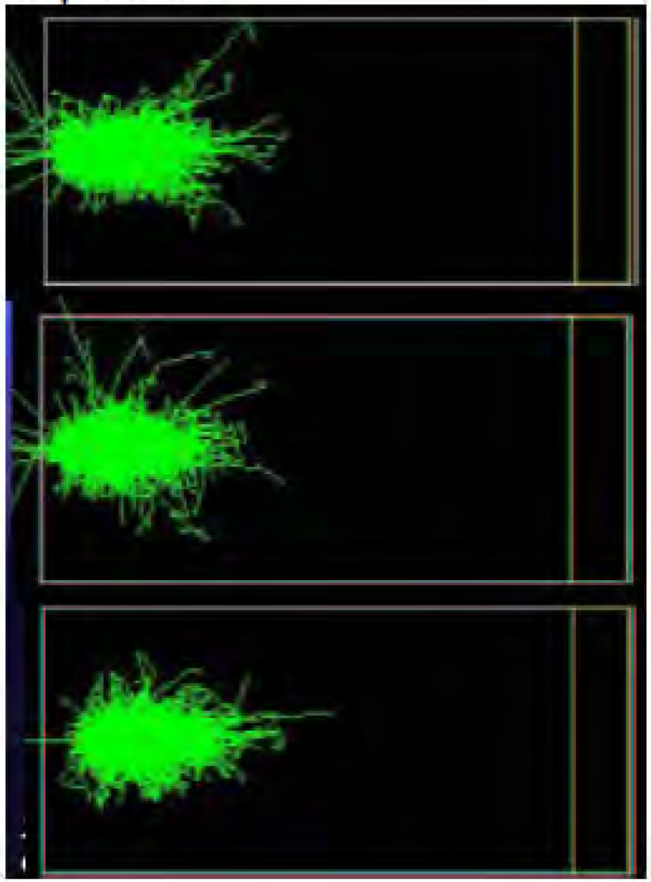

Electromagnetic calorimeters.

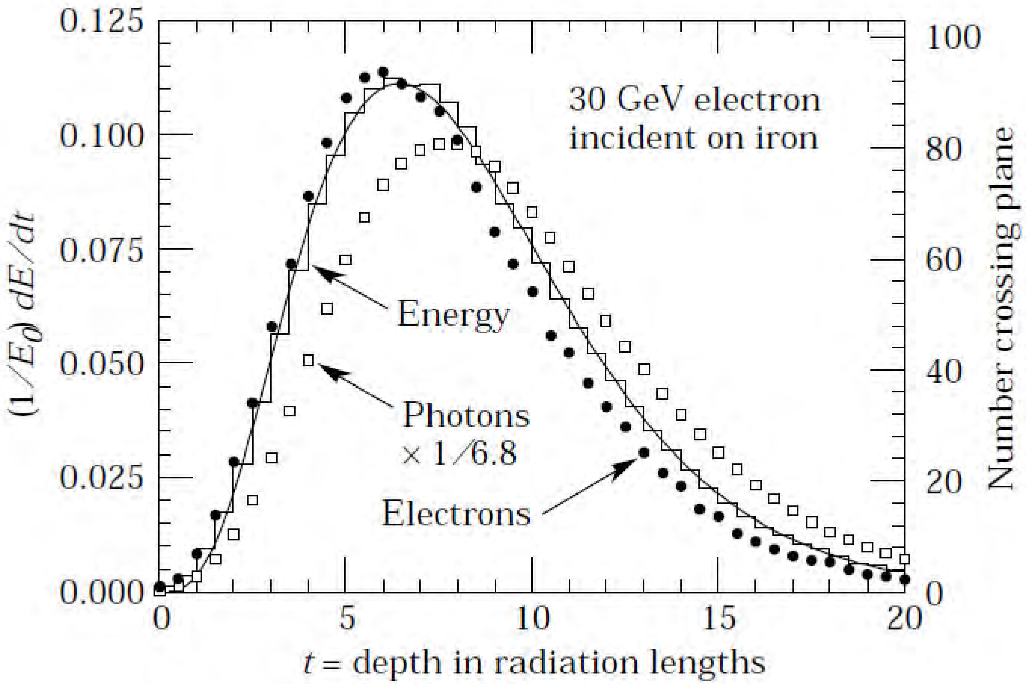

Figure 27.18: An EGS4 simulation of a 30 GeV electron-induced cascade in iron. The histogram shows fractional energy deposition per radiation length, and the curve is a gamma-function fit to the distribution. Circles indicate the number of electrons with total energy greater than 1.5 MeV crossing planes at $X_0/2$ intervals (scale on right) and the squares the number of photons with $E \geq 1.5$ MeV crossing the planes (scaled down to have same area as the electron distribution).

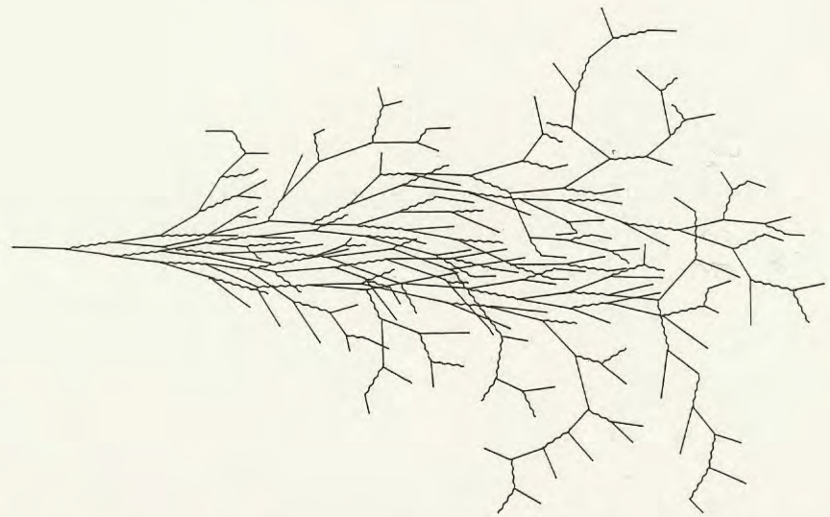

Fig. 7.20. Schematic representation of an electromagnetic cascade. The wavy lines are photons and the solid lines electrons or positrons.

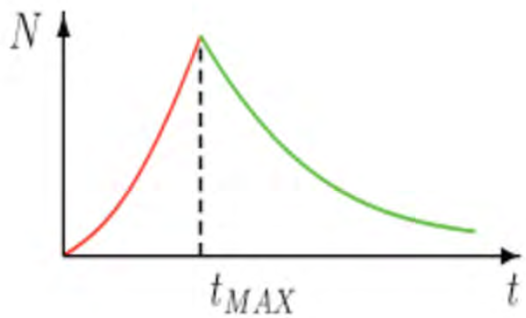

Figure 11.2 Shower profiles in lead. The number of electrons should be multiplied by a normalization factor of 0.79. (D. Müller, Phys. Rev. D 5: 2677, 1972.)

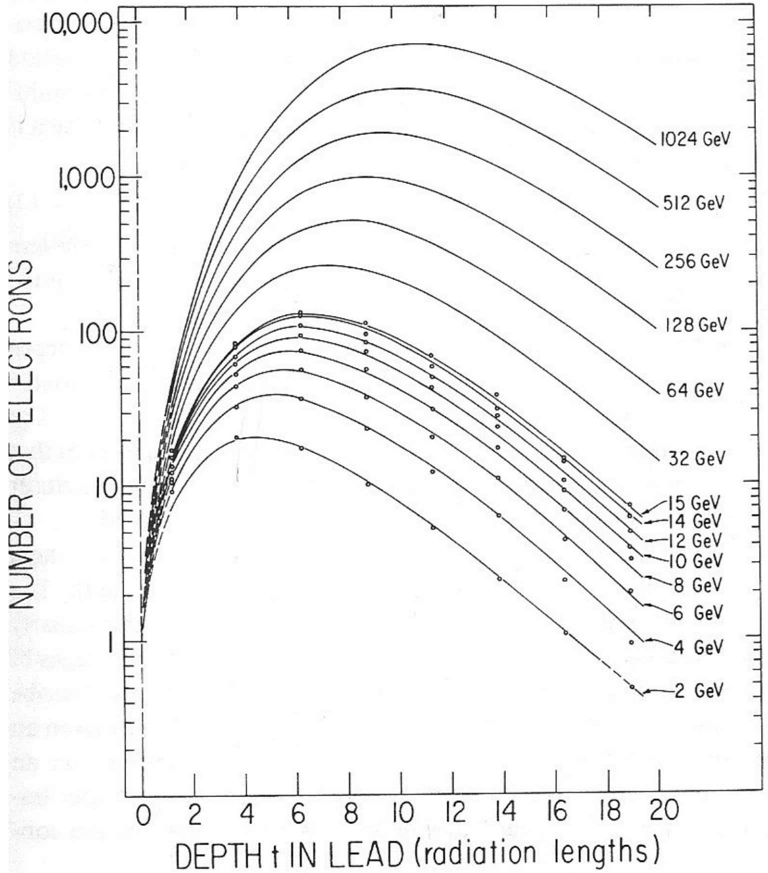

Figure 11.3 Longitudinal development of electromagnetic showers different materials. Right scale shows radii for 90% shower containmer (C. Fabjan and T. Ludlam, adapted with permission from the Annu Review of Nuclear and Particle Science, Vol. 32, © 1982 by Annu Reviews, Inc.)

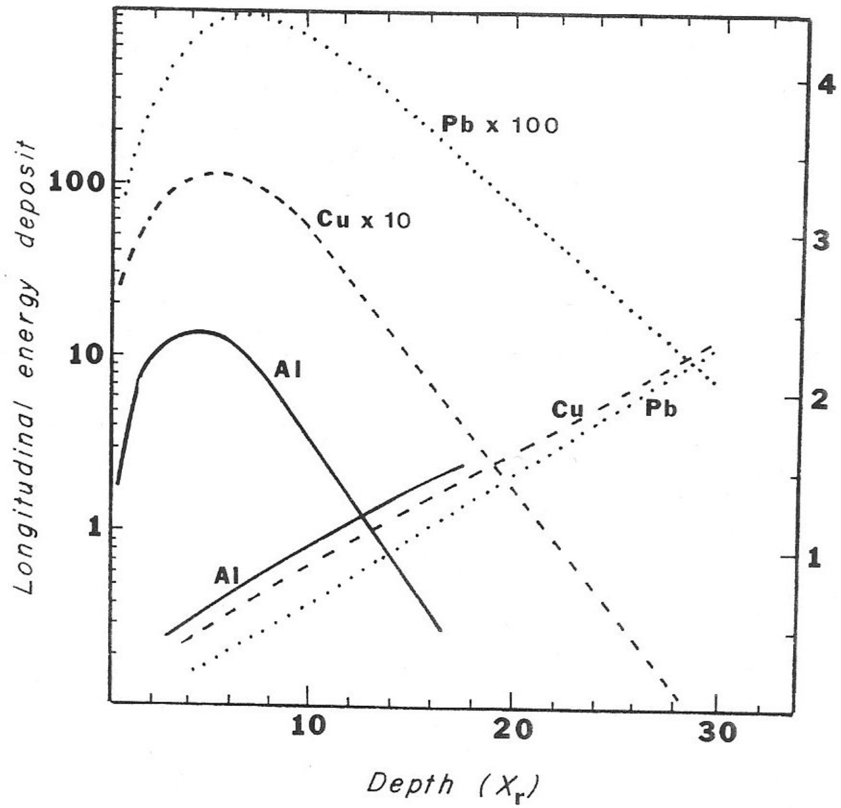

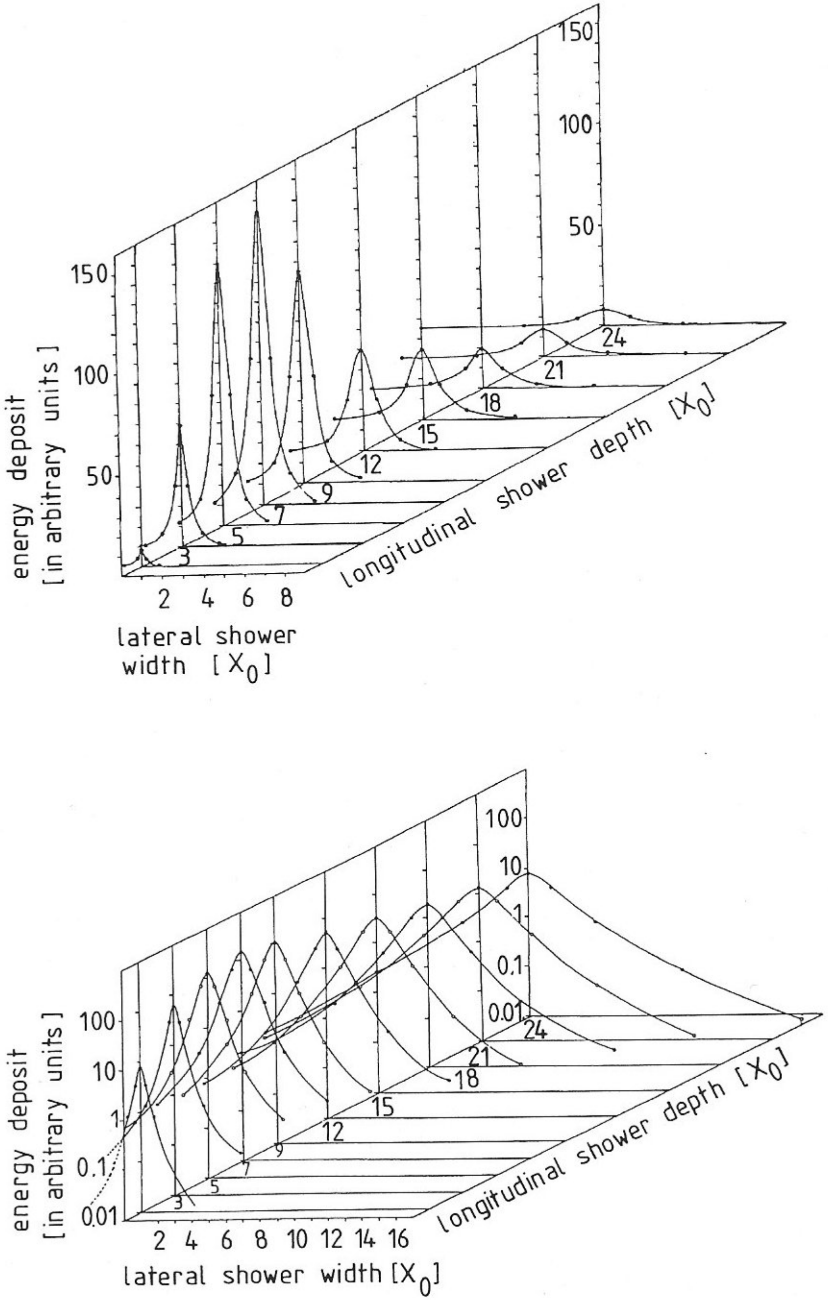

Fig. 7.23. Longitudinal and lateral development of an electron shower (6 GeV) in lead shown with linear and logarithmic scales (based on [504, 505]).

Electromagnetic calorimeters

- Basic readout types for sampling calorimeters

  - Metal-scintillator sandwich structure

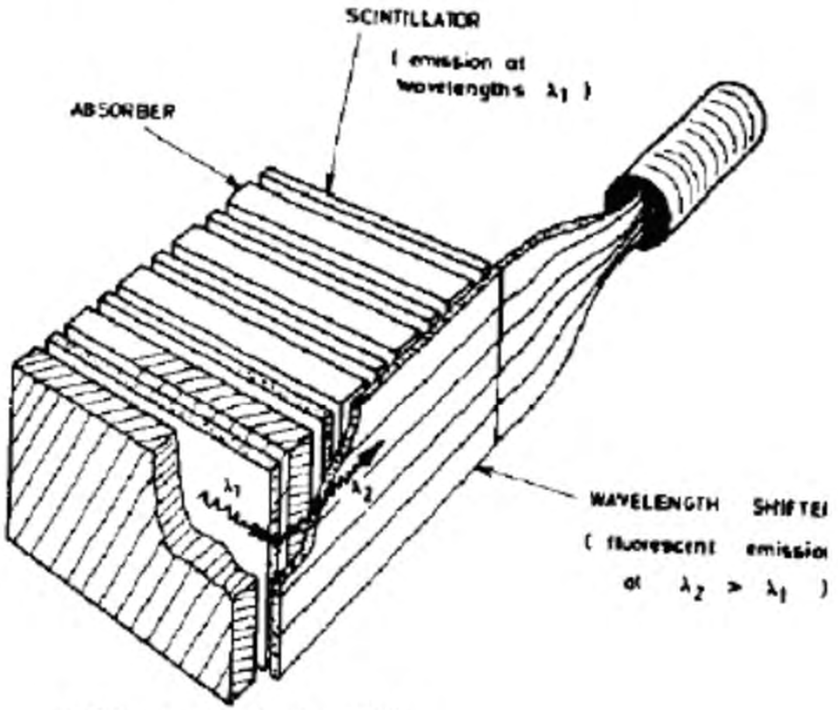

C. Fabjan and T. Ludlam, 1987

  - Metal-liquid argon ionization chamber

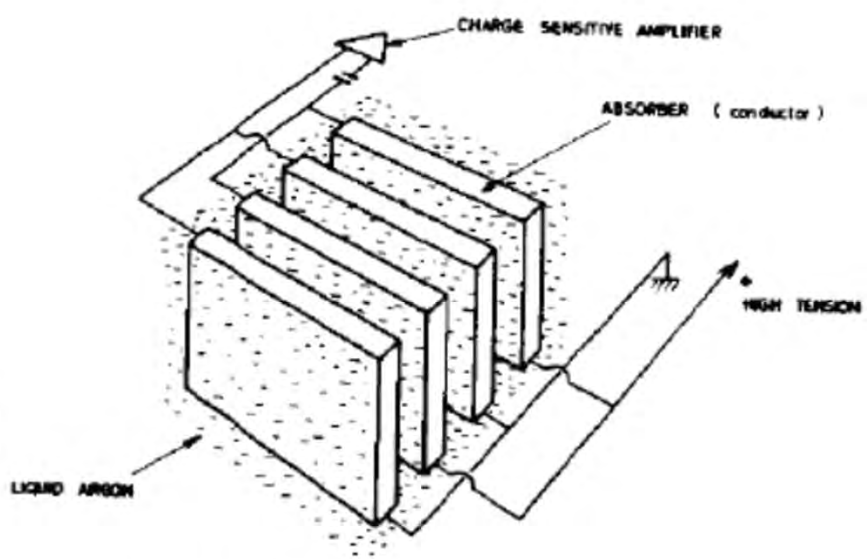

C. Fabjan and T. Ludlam, 1987

- **Energy resolution: Limitations**
  - Dead material effects

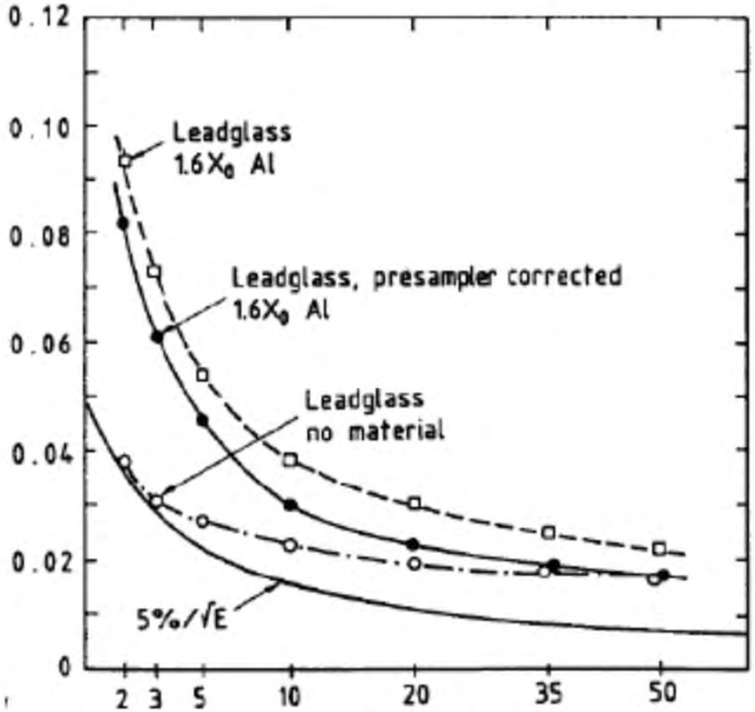

OPAL collaboration, C. Beard et al. NIM A 286 (1990) 117.

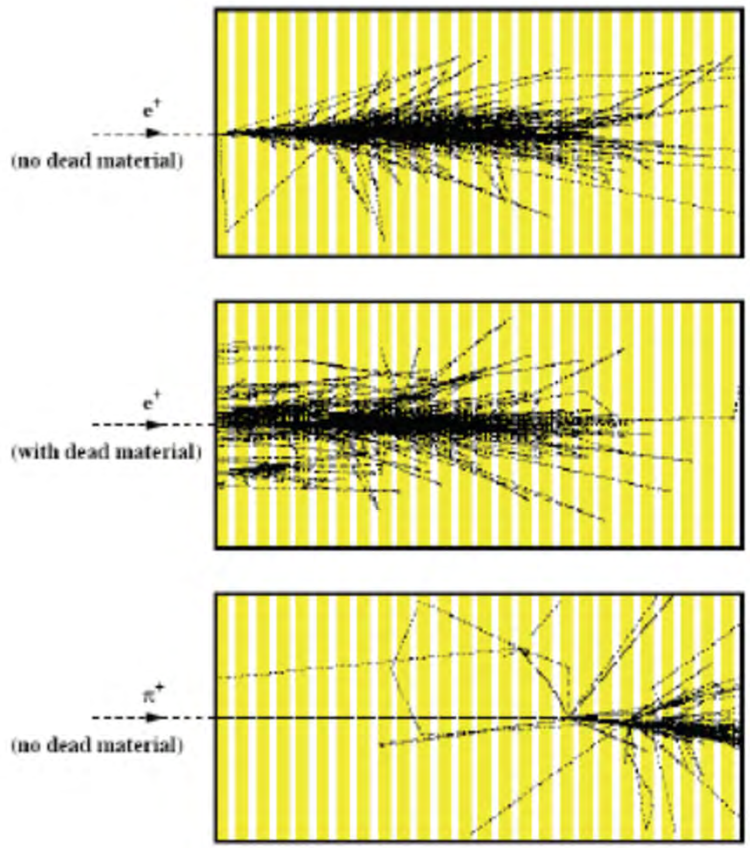

Shower simulation

EM calorimeters used for mass discrimination

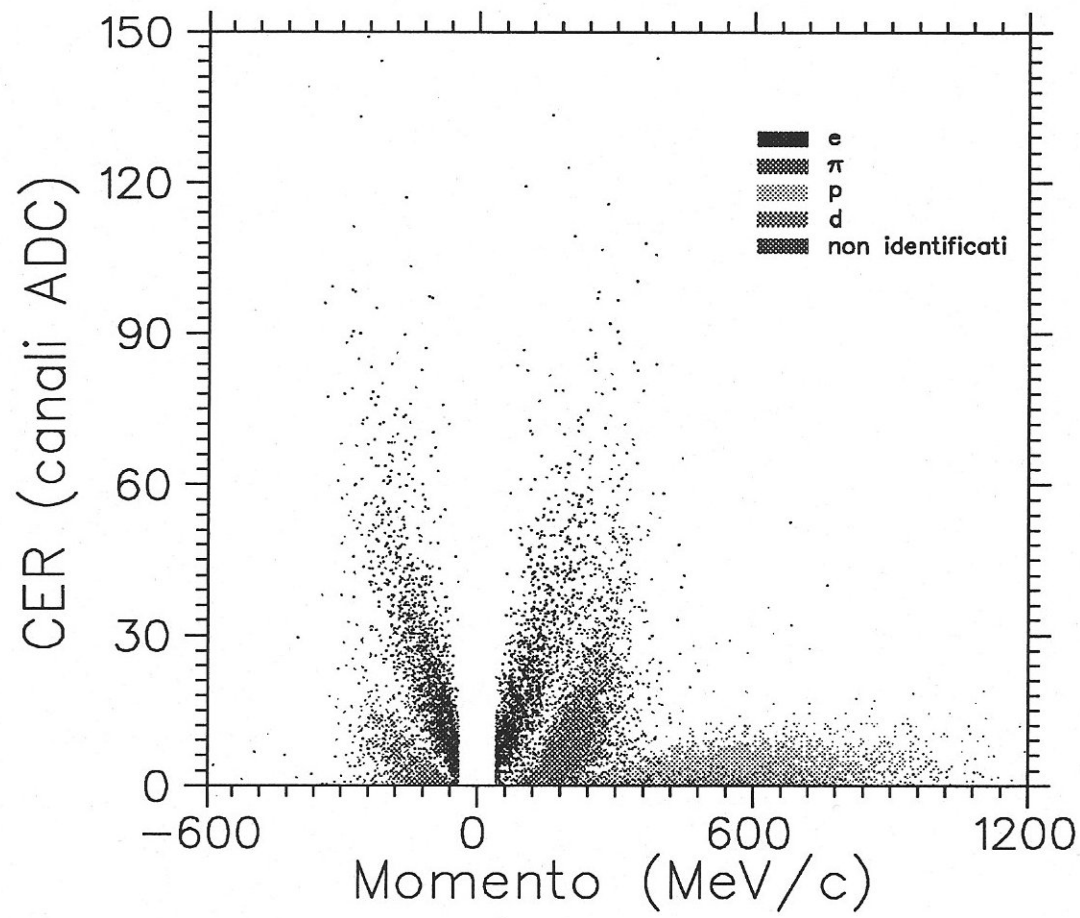

Figura 6.16: Distribuzione dei punti rappresentativi sullo scatterplot *(CER vs momento)* delle particelle cariche rivelate dallo spettrometro CHAOS, ottenuta dopo la procedura di identificazione. Nel grafico sono mostrate le particelle con tutti i gradi di identificazione (PID).

Hadronic showers

- **Hadronic shower development**
  - General comment: Complexity of of hadronic and nuclear processes produce multitude of effects that determine the functioning and performance of hadron calorimeters
    - Many channels compete in the development of hadronic showers
    - Larger variations in the deposited and visible energy
    - More complicated to optimize
  - Sizeable electromagnetic (e) besides hadronic (h) shower contribution mainly from π^0 decay (1/3 of pions)
  - Invisible energy due to delayed emitted photons in nuclear reactions, soft neutrons and binding energy
  - Visible energy smaller for hadronic (h) than for electromagnetic (e) showers: Ratio of response e/h > 1
  - Larger intrinsic fluctuations for hadronic than electromagnetic showers
  - Improvements: Increase visible energy to get e/h=1: Compensation (Compensation for the loss of invisible energy)!
  - Discussed instr. effects for e showers also hold for h showers

Step 1: Production of energetic hadrons with a mean free path given by the nuclear interaction length:

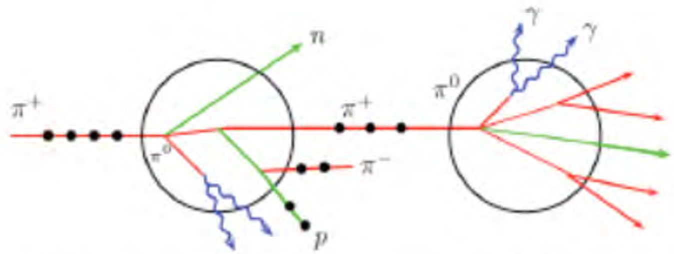

dE/dx nuclear cascade dE/dx nuclear cascade

Step 2: Hadronic collisions with material nuclei (significant part of the primary part of primary energy is consumed in nuclear processes):

Evaporation

Evaporation followed by evaporation

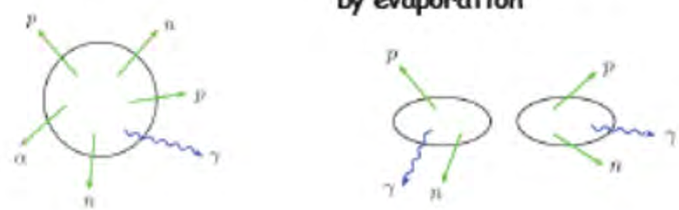

Processes contributing to the energy deposition in hadronic cal.

Table 11.2. *Average fractional energy deposition for a 10-GeV proton in an iron/liquid argon calorimeter*

Process	Percent of total
Secondary proton ionization	31.6
Electromagnetic cascade (π^0)	21.0
Nuclear binding energy plus neutrino energy	20.6
Secondary $\pi^{\pm}$ ionization	8.2
Neutrons with $E > 10$ MeV	4.9
Neutrons with $E < 10$ MeV	3.9
Residual nuclear excitation energy	3.7
$Z > 1$ ionization	2.4
Primary proton ionization	2.3
Other	1.4

Source: T. Gabriel and W. Schmidt, Oak Ridge National Laboratory report, ORNL/TM-5105, 1975.

Hadronic Calorimeters (are [very] difficult to model)

20 GeV π in copper (simulation)

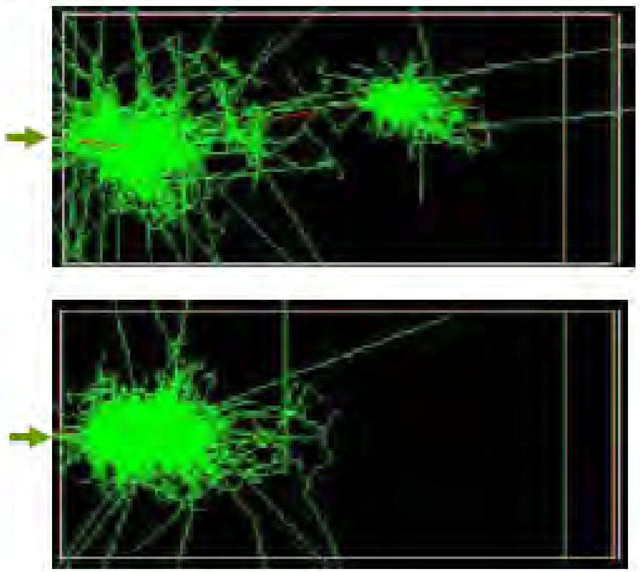

J.P. Wellisch

Hadron showers

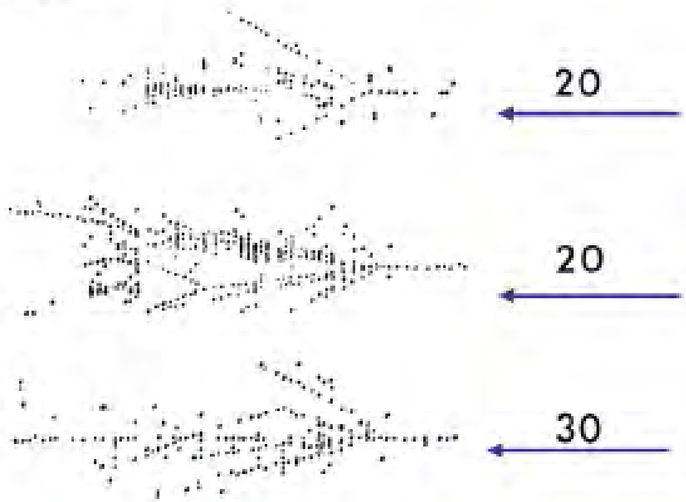

Hadronic Showers (π, n, p, ...)

Propagation : inelastic hadron interactions
$\rightarrow$ multi particle production
Nuclear disintegration

very LARGE

Neutrino

Weak interactions
secondaries : mostly hadrons

Nuclear Interaction Length λ_i

is the average distance a high-energy hadron has to travel inside a medium before a nuclear interaction occurs.

Probability not to have interacted after a path z $\quad P = e^{-z/\lambda_i}$

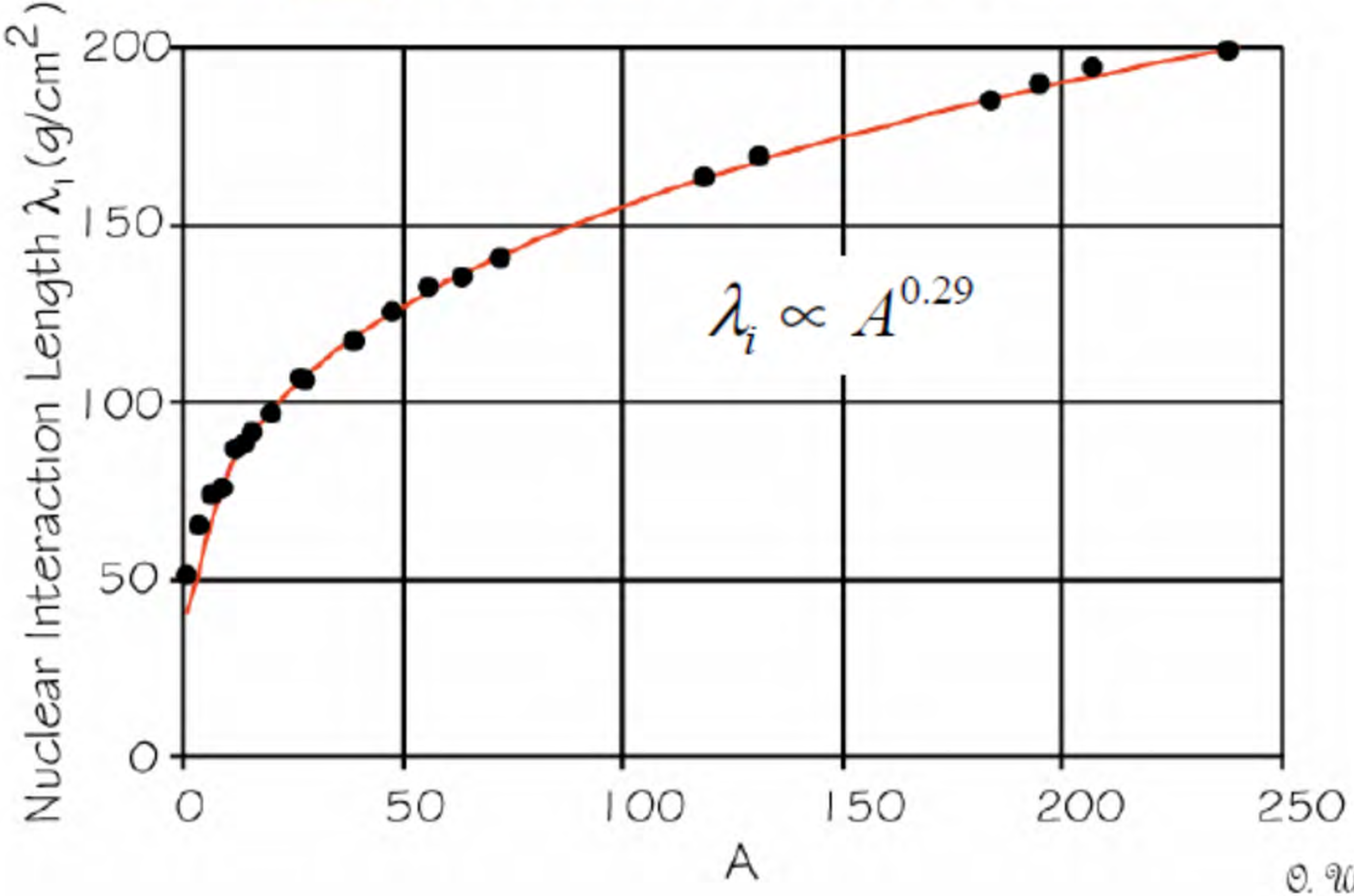

O. Ullaland/2006

Longitudinal distribution of energy in hadron calorimeter.

Fig. 6.6. Longitudinal distribution of energy deposited in a hadron calorimeter; Q_p is the energy deposited in counter p consisting of five layers with 2.5 cm iron and 0.5 cm scintillator each; $Q = \sum Q_p$. Measurements for π mesons of 15 GeV and 300 GeV [BL 82].